Medical Imaging of Microrobots: Towards *In Vivo* Applications

Azaam Aziz[1†], Stefano Pane[2,3†], Veronica Iacovacci[2,3], Nektarios Koukourakis[4,6], Jürgen Czarske[4,5,6], Arianna Menciassi[2,3], Mariana Medina-Sánchez[1*], and Oliver G. Schmidt[1,7,8]*

[1]Institute for Integrative Nanosciences, Leibniz IFW Dresden, Helmholtzstrasse 20, 01069 Dresden, Germany

[2]The BioRobotics Institute, Scuola Superiore Sant'Anna, Pisa 56025, Italy

[3]Department of Excellence in Robotics & AI, Scuola Superiore Sant'Anna, 56127 Pisa, Italy

[4]Chair of Measurement and Sensor System Technique, School of Engineering, TU Dresden, Helmholtzstrasse 18, 01069 Dresden, Germany

[5]Cluster of Excellence Physics of Life, TU Dresden, 01307 Dresden, Germany

[6]Center for Biomedical Computational Laser Systems, TU Dresden, 01062 Dresden, Germany

[7]Center for Materials, Architectures and Integration of Nanomembranes (MAIN), TU Chemnitz, Reichenhainer Strasse 10, 09107 Chemnitz, Germany

[8]School of Science, TU Dresden, 01062 Dresden, Germany

[†]Equal contributions

[*]Corresponding Authors:

Dr. Veronica Iacovacci (veronica.iacovacci@santannapisa.it)

Dr. Mariana Medina-Sánchez (m.medina.sanchez@ifw-dresden.de)

KEYWORDS: *medical microrobots, in vivo imaging, micromotors imaging, real-time tracking, swarm tracking, targeted therapy, target monitoring, microrobot actuation, in vivo navigation*

ABSTRACT

Medical microrobots (MRs) have been demonstrated for a variety of non-invasive biomedical applications, such as tissue engineering, drug delivery, and assisted fertilization, among others. However, most of these demonstrations have been carried out in *in vitro* settings and under optical microscopy, being significantly different from the clinical practice. Thus, medical imaging techniques are required for localizing and tracking such tiny therapeutic machines when used in medical-relevant applications. This review aims at analyzing the state of the art of microrobots imaging by critically discussing the potentialities and limitations of the techniques employed in this field. Moreover, the physics and the working principle behind each analyzed imaging strategy, the spatiotemporal resolution, and the penetration depth are thoroughly discussed. The paper deals with the suitability of each imaging technique for tracking single or swarms of MRs and discusses the scenarios where contrast or imaging agent's inclusion is required, either to absorb, emit or reflect a determined physical signal detected by an external system. Finally, the review highlights the existing challenges and perspective solutions which could be promising for future *in vivo* applications.

Scientists around the world have aimed for a long time at developing miniaturized robots that can be controlled inside the human body to aid doctors in identifying and treating diseases. The visionary idea of performing non-invasive medical interventions by using tiny machines, postulated by Albert Hibbs and Richard Feynman back in *1959,*[1] is not considered science fiction anymore, and is becoming a reality. These miniaturized robots, here called MRs are tiny structures with simple geometries such as rods, tubes, spheres, and helices, which can be propelled by chemical reactions,[2–9] physical fields,[10–21] motile cells or microorganism inclusion,[22–28] and which can perform several functions,[27,29–35] such as minimal invasive surgery,[13,36,37] sensing,[38–40] targeted drug delivery or diagnosis.[30,41] Precise control over MRs locomotion and function is necessary to enable target reaching and efficient task performance; however, fine control is possible only if information on MRs position and configuration is available. Few examples of MRs in living mice and small animals have been reported for cancer and bacterial infection treatments,[42–46] but the way ahead to the clinical practice and to high therapeutic efficiency is still long. In fact, despite a rapid development in the last decade, most of the MR applications demonstrated till now have been enabled by the use of optical microscopy in *in vitro* conditions and translating such approaches to an *in vivo* environment towards real medical applications is not straightforward.[47] Medical imaging techniques should be employed to visualize the physiological environment, including potential vascular routes and the target site for therapy, and for assessing the position of MRs in biological environment. In this framework, a wide plethora of medical imaging techniques are available. However, employing standard medical imaging techniques for microrobots localization is not trivial and many challenges still need to be faced in the attempt to identify the best compromise between spatiotemporal resolution, field of view (FoV), penetration depth and level of invasiveness associated with the imaging technique. The suitability of each imaging technique depends also on the working body districts and on the possible employment of swarm control strategies. For

example, organs such as the eye or the skin can be analyzed using imaging techniques with low penetration depths.[48,49] In contrast, applications such as cancer treatment[50] in internal organs or assisted *in vivo* fertilization,[12,22] just to mention some examples, require deep tissue imaging.

In this paper, we critically review the state of the art of MRs imaging in phantom, *ex vivo*, and *in vivo*, including both conventional and hybrid imaging techniques. A particular focus is given to the physics behind each technique in the attempt to unveil the opportunities and limitations of each imaging strategy with the aim to provide the readers with useful indications and guidelines to steer future research in the field of microrobotics. However, understanding the basic principles behind the different imaging strategies and analyzing their potentialities to resolve microscale structures in biological environment, will also be of interest for a wider healthcare research community interested in performing deep tissue imaging with high spatiotemporal resolution for investigating biological and synthetic mechanisms such as microcirculation, vascularization of implanted materials, cell migration, microrheology or any dynamic phenomena occurring at the micro and nanoscale.

Among "conventional techniques", optical, ultrasound, magnetic and radiation-based imaging methods are described, in particular when used to track medical MRs. Likewise, "hybrid techniques" such as photoacoustic (PA), and magnetomotive ultrasound (MMUS) imaging are reviewed. The review also deals with the suitability of each technique for single microrobot or swarm tracking and discusses the scenarios where contrast or imaging agents are required. Finally, some unexplored concepts combining different excitation sources (*e.g.* light, magnetic field, ultrasound) as well as different detection principles (*e.g.* acousto-mechanics, light reflection, wavefront shaping) are put into perspective, elucidating different means of imaging that can outperform current techniques in the future for MR-assisted theranostic applications.

CONVENTIONAL IMAGING TECHNIQUES

All imaging techniques share the same basic principle: a physical signal passes through the body/area under diagnosis and its interaction with the tissue causes transmission or reflection of the radiation which is then captured by a detector array and processed into an image pattern.[51] Different energy sources can be exploited ranging from electromagnetic fields (including light and high energy radiations) to ultrasound.

In this review paper, clinically established and widespread imaging techniques such as magnetic resonance imaging (MRI), ultrasound (US), optical and ionizing radiation-based techniques are defined as "conventional techniques" although they are continuously improving in terms of technical specifications for future potential applications. Based on the underlying physics, we classify the conventional techniques into (*i*) magnetic field, (*ii*) ultrasound, (*iii*) optical and (*iv*) ionizing radiation-based ones (**Figure 1A**). MRI and magnetic particle imaging (MPI) are described as magnetic field-based techniques whereas pulse-echo techniques, such as B-mode and Doppler-mode imaging, are included in the US-based techniques. Optical-based techniques to visualize MRs are classified into two groups, namely reflection-based imaging (RI) and fluorescence-based imaging (FI). Last, imaging techniques employing high energy radiation will be analyzed by describing in detail Computed Tomography (CT), X-rays, fluoroscopy, Positron Emission Tomography (PET) and Single Photon Emission Computed Tomography (SPECT) principles and employment in MRs localization and tracking. Although various other imaging techniques may be available, we discuss the most promising candidates for the localization and tracking of MRs in terms of three key parameters, namely spatial and temporal resolution as well as penetration depth (**Figure 1B).** Spatial resolution is the parameter which defines the minimal object size guaranteeing imaging or alternatively, which is the minimal distance possible between two objects to be discriminated from each other. Temporal resolution is the minimal time required

to complete the data acquisition needed to reconstruct one complete image of the object. Penetration depth is the measure of how deep the probing signal can penetrate into tissues and can be defined as the distance where the primary intensity is reduced to l/e (*i.e.* 37%) of the initial transmitted intensity. Additionally, another crucial parameter is the contrast resolution (or simply contrast), defined as the ability to distinguish between different levels of intensity in an image.

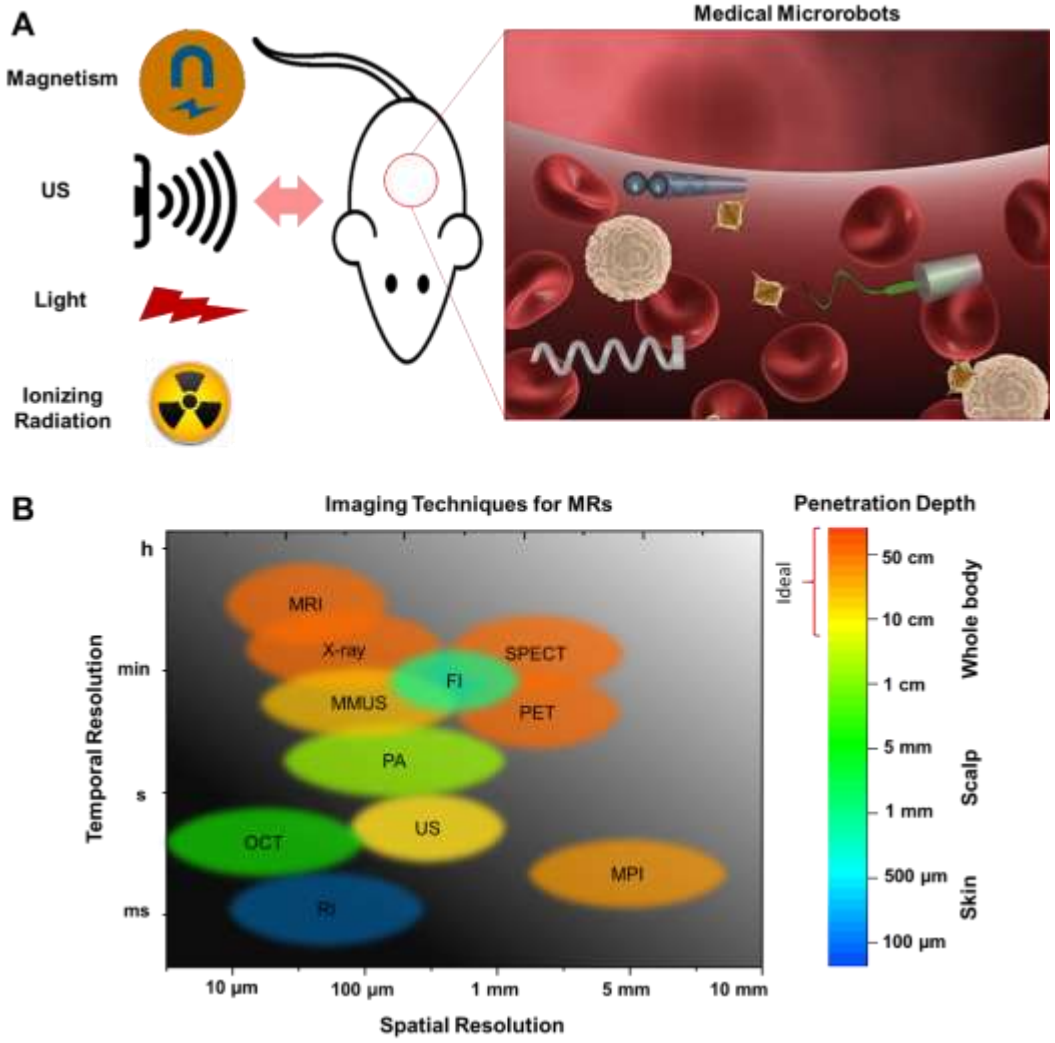

Figure 1. A) Imaging techniques to visualize and control medical MRs in living organisms. B) Spatial resolution, temporal resolution and tissue penetration depth overview of the most widespread biomedical imaging techniques: Magnetic Resonance Imaging (MRI); Magnetic

Particle Imaging (MPI); Ultrasound (US) Imaging; Reflection-based Imaging (RI); Fluorescence Imaging (FI); X-ray Imaging (X-ray); Positron Emission Tomography (PET); Single Photon Emission Computed Tomography (SPECT); Photoacoustic (PA) Imaging; Magnetomotive Ultrasound (MMUS); Optical Coherence Tomography (OCT). Dark gray region indicates the ideal scenario for spatial and temporal resolution for tracking medical MRs, and the ideal penetration depth is marked as yellow-orange color.

Magnetic Field-based Techniques

Magnetic field-based techniques are well-established and widely used in biomedical imaging to investigate the anatomy, physiology of the body and to detect pathologies including tumors, inflammation, strokes or abnormalities in the heart or blood vessels. Magnetic fields in the range of few Teslas can propagate in deep tissues and interact as non-destructive radio waves. These interaction phenomena range from electrodynamic exchanges to the generation of mechanical forces and torques, and can be translated into detectable electrical signals. Magnetic-based techniques allow functional (by using magnetic tracers) and anatomical imaging (thanks to the spin of hydrogen atoms abundant in soft tissues), as in the case of MRI, but also measuring the spatial distribution of specific materials, as for the scenario of MPI. These two techniques typically rely on expensive coil-based equipment and call for dedicated powering sources and cooling systems that significantly increase the complexity of the imaging apparatus. Two key features of magnetic techniques lie in the high penetration depth, especially in MRI due to the low attenuation of magnetic fields across tissues, and in the possibility to combine imaging and manipulation of MRs with the same apparatus.

Magnetic Resonance Imaging

MRI is particularly suitable to acquire 3D anatomical images of soft tissues and is used for this purpose in clinical practice. This can be achieved with a high spatial and temporal resolution with and without the use of specific contrast agents. Progress in MRI research has been tremendous in recent years, feedback control units have been significantly improved, and it has become one of the most appealing methods not only for medical imaging, but also for targeted minimally invasive therapies.[25,52,53] MRI is based on the principle of atomic spin relaxation. The term relaxation is used to describe the process by which a nuclear spin returns to thermal equilibrium after absorbing radio-frequency (RF) energy.[54] Three magnetic field stimuli are combined in MRI, namely a static magnetic field, electromagnetic RF signals and magnetic field gradients for localization (**Figure 2A)**.[55] In MRI the nuclear spins of hydrogen atoms, naturally abundant in tissues and biological materials, align under the effect of high intensity static magnetic fields (typically between 1.5 and 3 T). Pulses of radio waves are employed to excite the nuclear spin energy transition, which tend to realign with the static field in the process of relaxation. There are two principal relaxation components, *i.e.* longitudinal and transverse, related to the time constants T1 and T2, respectively (**Figure 2B)**. Magnetic field gradients allow for the localization of these signals in space.

By varying the parameters of the pulse sequence, different contrasts may be generated between tissues (or non-biological objects as MRs can be) according to the relaxation properties of the hydrogen atoms therein. Based on its operating principle and on the capability of the technique to detect almost any kind of material, MRI can be considered as a label-free technique not calling for the employment of dedicated contrast or imaging agents. However, when considering micro- and nanoscale objects, magnetic materials could be employed to increase the signal intensity and enhance image quality. Superparamagnetic and paramagnetic agents, based on gadolinium ion complexes or on iron oxide nanoparticles (NPs), are particularly important as MRI contrast agents

due to their high relaxivity (*i.e.* relaxation rate as a function of concentration). Magnetic materials subjected to the static magnetic field of a clinical MRI scanner produce a locally perturbing dipolar field with a shortening of the transverse relaxation time T2.[56] Based on the strength of the magnetic object, these distortions can be sufficiently large to detect MRs with overall dimensions smaller than the spatial resolution of any clinical imaging platform. Empirical observations suggest that an iron oxide particle distorts the magnetic field distribution over a region corresponding to about 50 times the particle size.[57] In this way, given that the typical size of a voxel in a standard 3T MRI scanner is about 500 μm, it is reasonable to say that single microrobot imaging could be foreseen for agents at least 10 μm in size (if magnetic properties are suitable enough) whereas swarm imaging appears more realistic for smaller or weaker magnetic microrobots.

In the early works by Martel and co-workers,[58–60] MRI was one of the initial clinical imaging techniques to be employed in the micro/nanorobotics scenario. In addition, MRI scanners produce strong magnetic fields and gradients which can be exploited for navigation of magnetic microrobots.[61–63] Martel and co-workers used MRI to image and steer magnetotactic bacteria and magnetic beads *in vitro* and *in vivo* (*e.g.* swine) across the vasculature (**Figure 2C-E**).[59,64,65] Interesting works from this group dealt with thermoresponsive hydrogel-based magnetic soft microrobots for targeted drug delivery.[66] In most cases, MRI was employed to image swarms of MRs (few μm in size each). Zhang and co-workers successfully employed MRI to track in rodent stomachs a swarm of magnetic helical microswimmers, obtained from *Spirulina* microalgae *via* a facile dip-coating process in magnetite (Fe_3O_4) suspensions.[43] They demonstrated the higher penetration depth enabled by MRI in comparison with fluorescence-based imaging. However, MRI imaging of single agents has been demonstrated only at the millimeter scale. For instance, Fatikow and co-workers exploited imaging artifacts produced by a single mm-scale ferromagnetic object for MRI-enabled closed loop control (tracking and navigation). Path planning algorithms based on

MRI data were integrated with a tracking module providing feedback on the position of the ferromagnetic object.[67] Reported works using MRI imaging to track MRs are summarized in **Table 1**.

Main challenges of medical MRI in the field of microrobotics are associated with spatial and temporal resolution. The spatial resolution is crucial for single microrobot visualization and for detecting events like target reaching, shape transformation or activation of drug delivery mechanisms. In MRI, the spatial resolution is directly proportional to the sampling rate of the relaxation signal, and inversely to FoV and slice thickness. Spatial resolution can also be improved by increasing the acquisition time, but that comes at a reduced framerate with inferior temporal resolution. In a previous study, the detection of a limited number of magnetic microrobots by MRI was achieved when increasing the acquisition time from seconds to few minutes.[68] For any specific application, an optimal compromise between spatial and temporal resolution needs to be identified.

Furthermore, when combining MR-based navigation and MRI, we should consider that different magnetic field signals are required for the two purposes. This calls for the necessity of implementing time-dependent multiplexed sequences in which navigation and imaging alternate and control relies also on pre-operative path planning. Possible delays and navigation instabilities produced by the switching between imaging and actuation could be minimized by appropriate processing algorithms or by employing multimodal imaging strategies, *e.g.* combining MRI with X-ray CT imaging.[69]

Alternatively, off-line imaging is often used to assess the targeting efficacy of microscale agents following the navigation phase and appears particularly interesting for MRs-based applications with low dynamics.

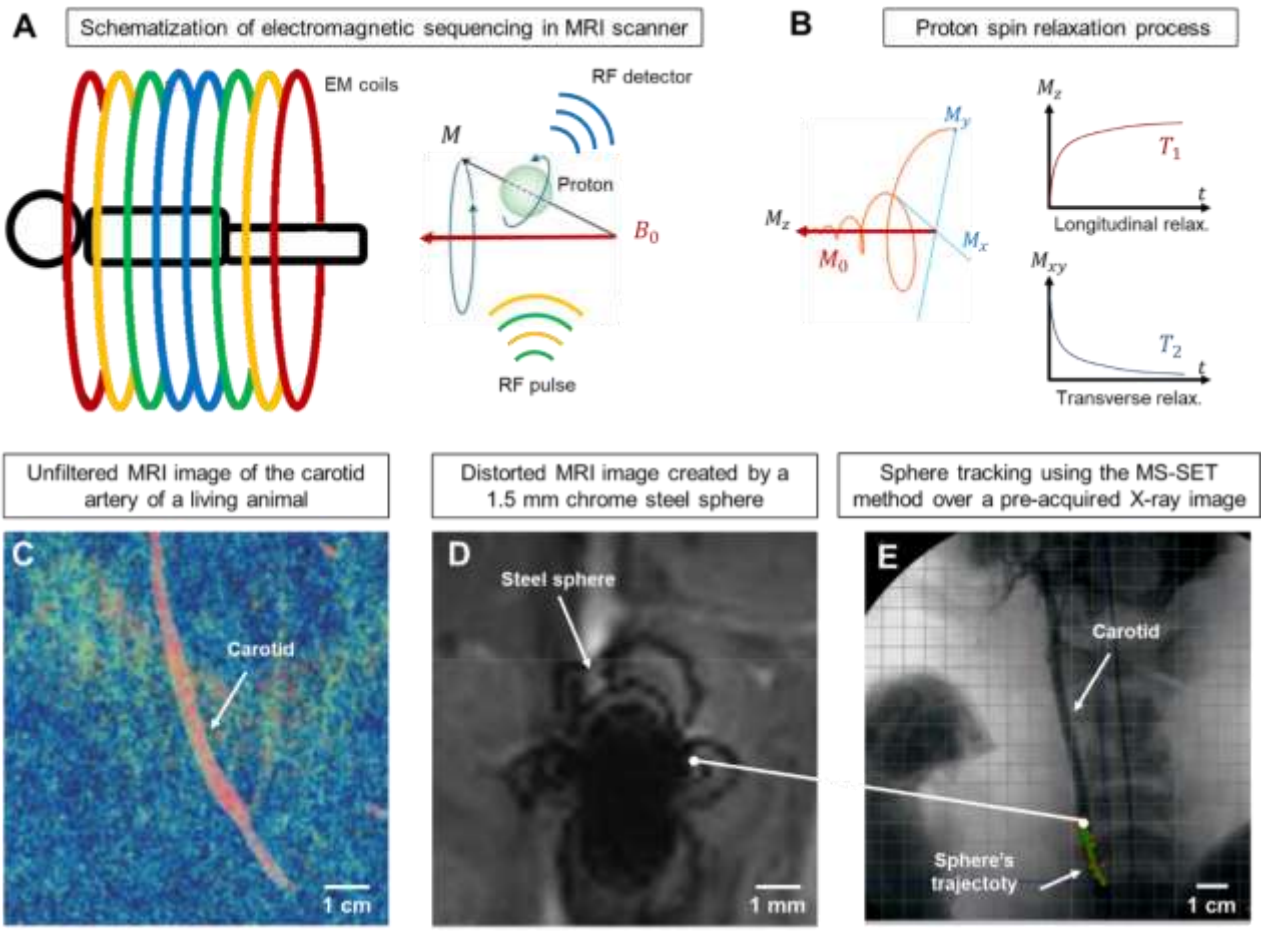

Figure 2. MRI tracking of microrobots. A) MRI scanner schematic and physical principle. B) Protons spin relaxation process and characteristic signals. C-E) Examples of MRI images from the state of the art showing both anatomical features and microrobots within the vasculature. Reprinted in part with permission under International Association of Scientific, Technical and Medical (STM) Publishers guidelines.[65] Copyright SAGEPub (2009). C) Unfiltered vasculature images (without any microrobot placed in the vessel). D) Distorted MRI image created by a 1.5 mm chrome steel sphere and E) Tracking of the same sphere over a pre-acquired X-ray image while being controlled at 24 Hz in the carotid artery of a living pig.

Magnetic Particle Imaging

MPI was proposed in 2001 by Bernhard Gleich and Jürgen Weizenecker.[70] The technique allows quantifying the presence of paramagnetic material in the FoV upon saturation of their magnetization. MPI cannot image tissue but can assesses the 3D distribution of paramagnetic material (*e.g.* NPs). To build an MPI scanner, two permanent magnets are arranged in a Maxwell configuration (*i.e.* opposing each other with identical poles) so that the magnetic field intensity is null in the central region of the arrangement, named the field-free point (FFP). Electromagnetic drive coils produce a time-varying magnetic field in the imaging area and dedicated pick-up coils detect changes in the NPs magnetization. Magnetization saturation of particles produces non-linear effects that generate harmonics which intensity is proportional to the particle's concentration. The static gradient field allows for spatial encoding and for detecting the origin of the signal. More specifically, at the FFP the particles magnetization is free to follow the drive field whereas outside the FFP the particles are saturated by the high-intensity static field, thus not producing any detectable signal (**Figure 3A**).

The FFP can be moved in space by introducing additional time-varying focus fields through the drive coils. This enables 3D volume scans with high temporal resolution within spherical workspaces of 10-20 cm in diameter. More specifically, MPI provides the capability of covering a volume similar to that of the entire heart or brain with more than forty 3D acquisitions per second. The spatial resolution of MPI increases with the intensity of the magnetic field gradient and with the particle's magnetic susceptibility. It lies in the range of one to few millimeters for currently developed MPI scanners.[71]

In the past decade, researchers have reported promising results regarding the use of MPI for the visualization and navigation of small magnetic devices. The high-intensity field gradients

generated within the scanner workspace allow to pull and actuate magnetic objects. In 2016, Gleich and coworkers demonstrated 1-D and 2-D closed-loop control and imaging of a millimeter-scale magnetic device using a prototype MPI setup.[72] Analogously to MRI, imaging and actuation require different drive field sequences in MPI. For this reason, controlled navigation is performed in a quasi-simultaneous manner by time-dependent multiplexed sequences in which actuation and imaging alternate. For this reason, even if imaging can be performed at very high frame rates, the achievable control frequency is limited by the time required by magnetic actuation.

In 2018, researchers from the same group developed a clinical scale system which was successfully used for 3D actuation of a centimeter-scale magnetic drill first in a phantom and then in *ex vivo* tissues.[73] This study highlighted how scaling up the workspace implies a reduction of the available spatial resolution, as a result of smaller magnetic field gradients. In 2018, Gleich and coworkers developed a human-sized MPI platform for brain applications (**Figure 3B**).[74] However, the achievable spatial resolution was about 10 mm, which is not suitable for microrobotic applications (**Figure 3C**).

Smart materials can improve the spatial resolution of MPI. In 2019, Bakenecker and coworkers reported a 3D-printed millimeter-scale helical swimmer (2 mm in length) and navigated it through a vessel phantom with an MPI scanner (**Figure 3D**).[75] The swimmer was coated with paramagnetic NPs (130 nm in diameter) to enable both imaging and navigation. With this setup, it was possible to obtain images of the navigated propeller (sub-millimeter resolution) at 10 frames per second (fps). In 2020, Griese and coworkers performed a comparative study in which swarms of different NPs were navigated through a vessel phantom in bifurcation flow by an MPI scanner.[76] They found dextran-coated iron oxide NPs with 250 nm diameter to provide the best compromise in terms of magnetic manipulability and imaging performance.

Overall, fast localization and strong forces due to the high field gradient render an MPI system as a good platform for image-guided steering of magnetic devices. Nevertheless, some limitations still hamper the translation of this technology into clinically-relevant scenarios. On one hand, more research efforts are needed to scale up the platforms and to enable human-sized workspaces, while guaranteeing good imaging performances. On the other hand, the spatial resolution seeks for improvement (a few millimeters with current platforms). Innovative solutions are required to progress in this direction, both in the design of high gradient selection fields and in the development of suitable materials with steeper magnetization characteristics.

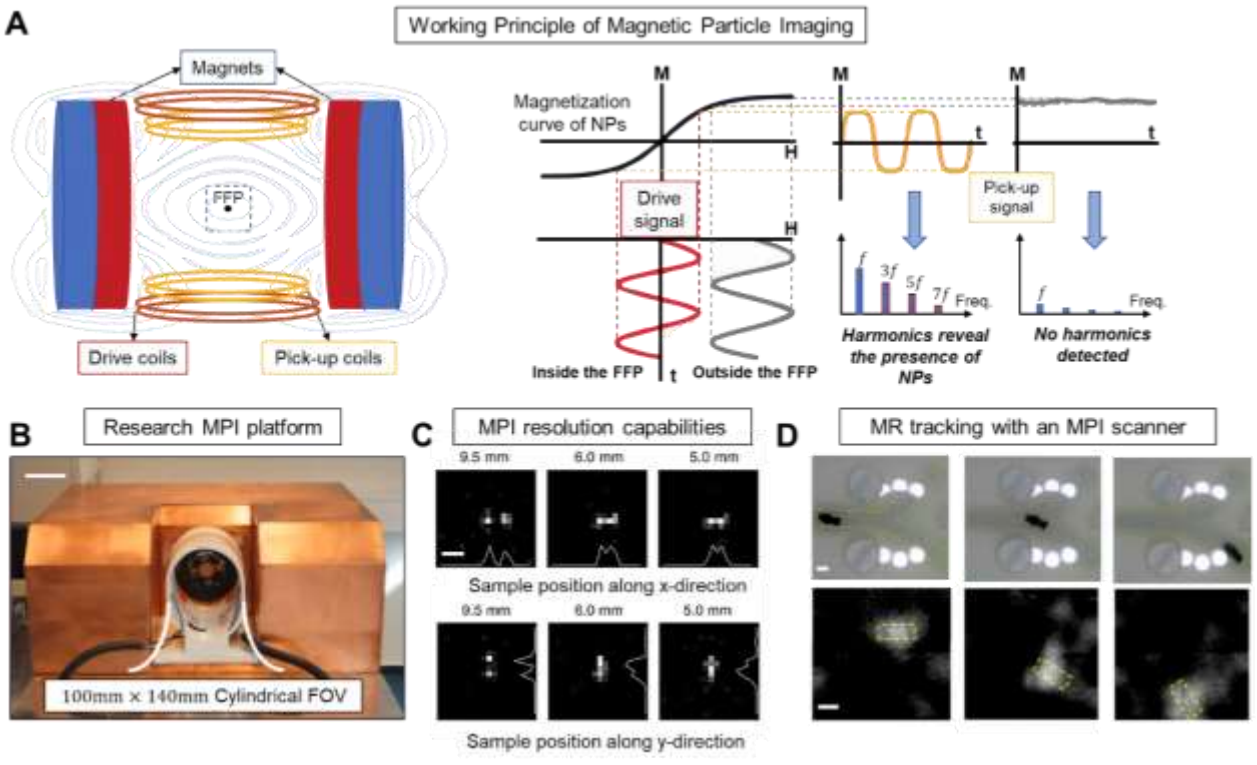

Figure 3. Magnetic particle imaging for the tracking of microrobots. A) Schematic of an MPI scanner and description of the working principle. An FFP is obtained through opposing magnets and allows to excite, through dedicated drive coils, the non-linear response in magnetization of paramagnetic NPs. The detection of harmonics in the magnetization signal, measured by pick-up coils, reveal the presence of paramagnetic NPs in the FFP. B) Human-sized MPI scanner for brain

applications with cylindrical FoV of 100 mm diameter and 140 mm height. Scale bar is 50 mm. C) Spatial resolution capabilities for which objects closer than 10 mm cannot be resolved properly. Scale bar is 10 mm. B-C) Adapted with permission under a Creative Commons CC-BY License from "Human-Sized Magnetic Particle Imaging for Brain Applications".[74] Copyright 2019 Springer Nature. D) Simultaneous navigation and localization of a millimeter scale microrobot through an MPI imaging platform (10 fps) and comparison with optical images. Scale bar is 4 mm. Adopted with permission.[75] Copyright Elsevier (2019).

Ultrasound-based Techniques

Amongst conventional techniques, US-based imaging stands as one of the most promising solutions for providing real-time feedback on microrobot position in deep tissue. It is a mature technology regularly used in clinical settings for diagnostic purposes. Compared to other conventional techniques, US combines high spatial and temporal resolution with minimum adverse effects on tissues and lower equipment cost. In US imaging, pulses of pressure waves are emitted by a piezoelectric transducer. When the waves encounter acoustic impedance discontinuities, they are partially scattered back towards the source.[77] The backscattered echo signal is registered by the transducer and can be processed to extrapolate information regarding the whole journey of the transmitted wave. Several US beams can be independently shot and registered back by an array of piezoelectric elements (US probe) to acquire adjacent scan lines which are then combined to reconstruct a 2D tomographic image, also known as a *frame*. In this review, we are going to discuss two different established US imaging modalities, namely B-mode and Doppler, which look particularly suitable for MR tracking.

B-mode Ultrasound Imaging

B-mode US is a pulse-echo imaging modality in which a pulse wave is transmitted by the US probe and the echoes generated by the interaction of the wave with the propagating media are processed to reconstruct an image of the insonated region (*i.e.* the region exposed to ultrasound). Assuming to transmit a sinusoidal pulse along a single scan line, the detected echo $E^*(t)$ can be expressed as:

$$E^*(t) = A(t) \cdot \mathrm{e}^{j(2\pi f t + \varphi(t))} \quad (1)$$

where $A(t)$ is the amplitude of the signal, f is the carrier frequency of the transmitted pulse and $\varphi(t)$ is the phase. The instantaneous amplitude $A(t)$, also known as the envelope of the signal, carries information about the pressure intensity that is locally backscattered by all objects along the path of the scan line. In brightness-mode (B-mode) imaging, $A(t)$ is converted into brightness levels to create a contrast image of the object (**Figure 4A**). When propagating in human tissues, US waves are strongly absorbed by bones (producing acoustic shadows) and highly reflected by air sacs. Due to its strong echogenicity (*i.e.* the property of backscattering US waves), the air is generally used as a contrast agent, for instance in the form of microbubbles. These are micron-sized spheres consisting of a gas core surrounded by a lipid shell which act as echo-enhancers.[78]

In B-mode imaging, the temporal resolution depends on the speed of sound in the medium (about 1500 m/s in soft tissues)[79] and on the FoV. Typical frame rates are in the order of 50-100 fps, while greater rates are achieved by plane wave imaging (>1000 fps).[80] The spatial resolution is defined by two parameters, namely axial and lateral resolution. The lateral resolution depends on the geometry of the US probe since it is related to the distance between the piezoelectric elements of the probe array. Axial resolution is related to the wavelength of the transmitted pulse (typically 100-500μm) and thus to both the characteristics of the transducer (center frequency) and the

properties of the medium (speed of sound). Due to wave diffraction, objects with characteristic dimensions comparable to the US wavelength are not well resolved. Ideally, axial resolution is defined by one half of the transmitted pulse wavelength. However, as a result of the combined effect of the physical processes involved (*i.e.* scattering and diffraction) and of the reconstruction procedure (*e.g.* imaging artifacts), the axial resolution of a B-mode image is usually worse than the ideal value.[81] A higher axial resolution can be obtained by increasing the transmission frequency, yet at the expense of the penetration depth (wave attenuation increases with frequency). Altogether, axial resolution can vary between hundreds of micrometers at 3-4 cm depth for 12-15 MHz US waves as those employed in Doppler-mode diagnostics, to millimeters at 20 cm depths for 3-5 MHz US waves, generally used in standard abdominal B-mode imaging.[82]

In the past few years, researchers have accomplished encouraging results in the localization and tracking of microrobots through B-mode imaging. In 2014, Misra and coworkers demonstrated that point-to-point control of a magnetic sphere (100 μm in diameter) could be achieved with position feedback extrapolated from B-mode images.[83] The authors reported an average position tracking error about half the microsphere size while navigating it in 2x2 cm arena. The same setup was used for tracking the trail of bubbles (spot size of ~300 μm) from a single self-propelled microjet *in vitro* with a characteristic length of 50 μm (**Figure 4B**).[84] To localize such a small microjet in the imaging plane, they exploited the echogenicity (*i.e.* characteristics of large wave reflection) of gas bubble trails produced by catalysis-based propulsion. However, the average position tracking error reported in this case was $250.7 \pm 164.7\ \mu m$, about 5 times the characteristic length of the micro-motor. To achieve better performances, in 2018 they developed a model-based tracking system able to achieve ultra-fast localization of millimeter-scale hydrogel grippers from B-mode images with an average position tracking error of $25 \pm 7\ \mu m$ (over one percent the dimension of the

gripper).[85] The same group recently demonstrated 3D position control of a magnetic sphere (800 µm in diameter) under US guidance.[86] To achieve 3D localization with 2D US tomographic images, the transducer was swept along the vertical direction to identify the horizontal plane containing the microrobot. The target plane (2D image) was thus processed by a tracker to extrapolate the remaining two coordinates. Promising results were reported also in *ex vivo* studies where different tasks of millimeter-scale robots were monitored through B-mode images. Qiu and coworkers exploited B-mode images for the localization of a helical propeller (characteristic length of 2 mm) moving in rat liver.[87] Cappelleri and coworkers used B-mode imaging to monitor a sub-millimetric tumbling microrobot capable of releasing the therapeutic payload in the dissected colon.[88] Sitti and coworkers used B-mode images to visualize the multimodal locomotion of a milli-robot within *ex vivo* chicken tissue.[14] However, none of these microrobot was smaller than 800 µm.

Recently, B-mode imaging has been successfully employed in microrobot swarm tracking.[89–91] Due to their enhanced area density, swarms of microrobots have shown very good contrast properties when imaged in B-mode.[92] In 2018, Zhang and coworkers reported the controlled navigation of a rotating colloidal swarm of paramagnetic NPs in a centimeter-scale arena, using B-mode images. They found the dynamic equilibrium conditions of the swarm to produce periodic changes in their contrast. These changes can be used to discriminate the swarm from other elements in the image. In addition, they demonstrated how the centripetal forces of the rotating swarms can be exploited to trap tunable concentrations of contrast agents (*e.g.* microbubbles) in their cores.[93] This feature can be exploited to further enhance the contrast properties of microrobotic swarms under B-mode imaging. In more recent studies, the same group exploited B-mode images to localize swarms of microrobots *ex vivo* in the bovine eyeball (**Figure 4C**) and swine bladder.[94,95]

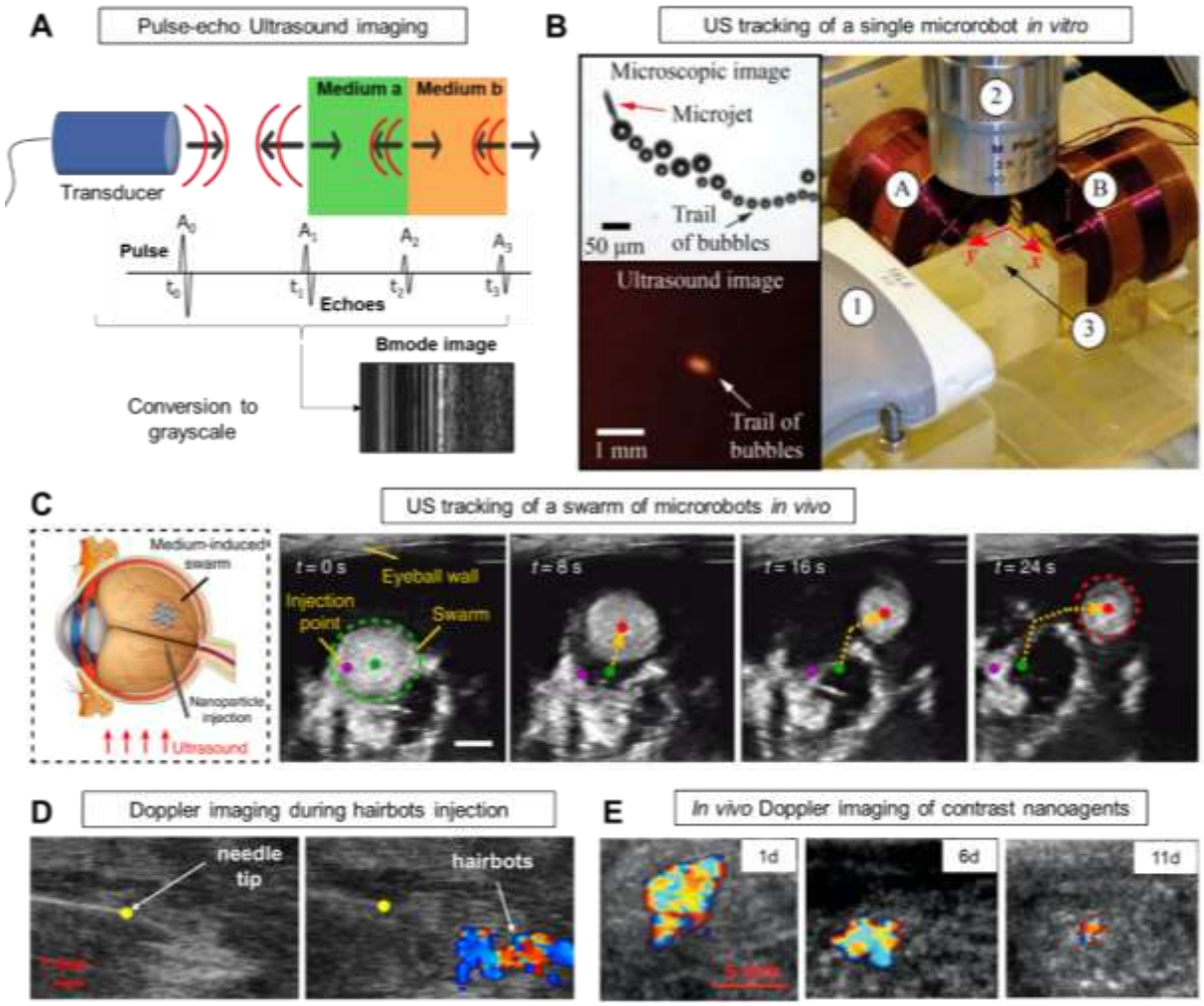

Figure 4. US imaging for the tracking of microrobots. A) Physical principle of pulse-echo US imaging and B-mode image reconstruction from backscattered waves. B) The reported results of controlling a single self-propelled microjet with B-mode images. Electromagnetic coils A and B enable microjet steering in the arena (3). An optical microscope (2) allows for calibration of the US tracking system, which features a high-resolution probe (1). Reprinted with permission.[84] Copyright IEEE-RAS (2014). C) Recent results in tracking a microrobotic swarm *ex vivo* in bovine eyeball. Injected NPs assemble into swarms due to magnetic manipulation and are navigated under US guidance. Reprinted in part with permission under a Creative Commons CC-BY License from "Active Generation and Magnetic Actuation of Microrobotic Swarms in Bio-Fluids".[94] Copyright 2019 Springer Nature. D) Doppler imaging of hairbots suspension after injection in *ex vivo* chicken

breast. Reprinted in part with permission.[96] Copyright Elsevier (2019). E) *In vivo* color Doppler images of tissue perfused with hollow silica nanoshells one, six, and eleven days after injection. Reprinted with permission.[97] Copyright Wiley (2015).

All these studies showed promising results *in vitro* and *ex vivo*, both for single microrobots and for collective swarms imaging. Nonetheless, the use of such methods in the biomedical scenario still requires the scientific community to address important bottlenecks. Above all, typical materials employed for fabricating microrobots show weak echogenicity. In the majority of the reported works, the MRs were localized within scarcely echogenic and still media (*e.g.* glycerol, vitreous humor) to improve the relative contrast of the objects to be tracked. On the other hand, human tissues show high echogenicity and are subjected to physiological motion (*e.g.* heartbeat, breathing). In such environments, the proposed tracking strategies may not be able to discriminate the target microrobot from the surroundings. In this regard, future research should focus on the development of smart processes for functionalizing the microrobots with contrast agents, *e.g.* microbubbles and/or gas vesicles to discriminate them from the surrounding environment. In addition, due to their small size, B-mode imaging of microrobots requires high resolution US settings which imply high transmitting frequency and thus low penetration depth, as a result of wave attenuation. In the majority of the reported works spatial resolution in the range of 100 μm was enabled by US transducers operating around 15 MHz which are limited to penetration depths of 3-4 cm, thus not suitable for biomedical tasks in deep tissues/organs. Breaking the resolution/penetration depth trade-off is a grand challenge towards the translation of US technologies for microrobotic applications.

On one hand, enhanced penetration depth could be achieved with passive US mode. With such a technique the microrobot itself acts as an US emitter by incorporating a micro-transducer (*e.g.* a

cantilever) in its architecture.[98] The emitted signal can be tracked through the body by placing receiver antennas around the patient.[99,100] In principle, since the ultrasonic signals only need to travel through the media once, this approach offers twice the penetration depth than pulse-echo mode. However, it needs sufficient energy at the microrobot location to generate appropriate US emission.

Alternatively, ultrasound localization microscopy (ULM) is a promising approach to achieve super-resolution. In ULM, the US signal scattered by microbubbles is processed along thousands of acquired frames to resolve images below the acoustic diffraction limit. With this technique, Lin and coworkers obtained US images with a pixel size of 10x10 μm using a 8 MHz transducer (featuring a diffraction limit of 100 μm).[101] Although promising, ULM has some bottlenecks for real-time MRs tracking. First of all, it is strongly dependent on a high dosage of contrast agent, not easily equipped on board a MR and secondly, it features poor temporal resolution. In fact, each ULM image was processed from 8000 acquired US frames, meaning more than a minute of acquisition with standard settings. Yu and coworkers[102] proposed a deconvolution method with which they reduced the acquisition time for each ULM image to about 6 s and other groups are working in the same direction,[103–105] but more efforts are required to make this method real-time.

Doppler Imaging

This US-based imaging technique relies on the Doppler effect, by which US waves that interact with moving objects experience a shift in their travelling frequency. More specifically, if two pulses are shot consecutively with a certain pulse repetition frequency (PRF) and interact with an object that has moved in the direction of wave propagation, the two echoes will show a difference in travelling frequency that is linearly related to the velocity of the moving object. This effect applies to all motion directions by considering their projection along the wave propagation direction. The

Doppler signal is extracted through quadrature demodulation techniques[81] and is converted to a measure of the velocity of the imaged objects. The PRF, which relates to the temporal resolution is actually the Doppler signal sampling rate. According to the Shannon theorem such sampling rate sets the maximal detectable Doppler shift. In the past years, Doppler imaging has been used for the visualization and control in 3D of vibrating tethered robotic devices such as microneedles[106] and instruments for cardiac interventions.[107] More recently, the use of this technique in microrobotic applications has been investigated. In 2019, Sitti and coworkers proposed *hairbot*, a microscale device derived from hair tissues.[96] The functionalization of such devices with superparamagnetic iron oxide NPs (SPIONs) enabled the interaction with stem cells in microenvironments through magnetic actuation. Doppler imaging was used to image the *hairbots* after injection in *ex vivo* chicken breast (**Figure 4D**). Other studies reported promising results in the fabrication of nanoagents for continuous Doppler contrast. Liberman and coworkers synthesized gas-filled silica nanoshells that can be detected *in vivo* using color Doppler imaging with great lifespans (over 11 days) (**Figure 4E**).[97] These studies highlighted how, at least in principle, microrobots could be functionalized with Doppler contrast agents to achieve robust localization in tissues. Unlike B-mode imaging, the Doppler principle does not involve the amplitude of backscattered US waves, thus making it an effective tool for detecting moving objects in dynamic and echogenic environments, as body tissues are. The works related to US imaging (B-mode and Doppler) of MRs are summarized in **Table 1.**

Optical-based Techniques

Optical imaging utilizes non-ionizing radiation sources such as lasers or LEDs. Such techniques are relatively fast, safe and low cost and offer high spatial (order of few μm) and temporal (order of millisecond to seconds) resolutions. However, most optical techniques suffer from low penetration depth in biological tissues and are still limited to the investigations at sub-surface

levels, typically between hundreds of micrometers and rarely beyond 1 mm deep.[108,109] Light penetration into tissues is limited by scattering and absorption at different biomolecules and endogenous chromophores and varies with tissue properties. These properties can be described by the mean free path (MFP) which is the average distance a photon travels between two scattering or absorption events and is defined as:

$$\mathrm{MFP} = \frac{1}{\mu_s} + \frac{1}{\mu_a} \quad (2)$$

where μ_s and μ_a are the scattering and absorption coefficients, respectively.[109]

One strategy to overcome the limited penetration depth of optical techniques is to choose an appropriate wavelength window which can significantly reduce the tissue autofluorescence and light absorption. It is the case of the two biological windows in the NIR range respectively at 650-950 nm (NIR-I) 1000-1350 nm (NIR-II). For higher penetration depths, the use of wavelengths from the second biological window is desirable as it has been demonstrated elsewhere.[110] Hence, in the appropriate wavelength range, μ_s is much larger than μ_a for most of the tissues *e.g.* muscle, brain, breast and lung tissues, and the MFP can be approximated to $1/\mu_s$. Scattering in biological tissues occurs predominantly in the forward direction (direction in which the light strikes the tissue). This is considered by the anisotropy factor "g" which defines the degree of forward scattering (g=1 meaning the total forward scattering and g=-1 the total backscattering). Typical values for biological samples are in the range of g~0.9. The transport MFP (TMFP) considers the MFP and the average angle in which photons are scattered and is linked to the MFP by the reduced scattering coefficient $\mu_s' = \mu_s(1-g)$. It is defined as TMFP = $1/\mu_s'$.[109]

Another strategy to improve the penetration depth is to tune the emission features of target objects (*i.e.* MRs) by incorporating dedicated contrast agents or labels. For the sake of clarity in the

classification, we have organized the optical imaging techniques used for MRs tracking into reflection-based and fluorescence-based techniques (see **Figure 5A, i-ii**).

Reflection-based Imaging

Optical techniques are widely used in body districts where the scattering of tissues is relatively low, *e.g.* in ophthalmology, sub-skin intervention and small animal experiments. As the penetration depth of light in tissue is comparably small, optical techniques are mostly used in reflection rather than transmission configuration, meaning that the illumination and detection are done with a single-sided optical access to the sample. RI does not rely on the emission of a fluorescent probe, but on the intrinsic reflection or backscattering properties of the sample. NPs or thin metal layers incorporated on target samples can be used to enhance signal reflectivity. In this regard, gold (Au) is one of the most suitable materials for its biocompatibility and high reflectivity over a broad spectral range.[111] However, when scattering scrambles both the illumination and the backscattered light, a high amount of background light occurs, which strongly reduces the signal to noise ratio (SNR). In the worst case, the scattered light saturates the detector and no sample information can be recorded. To reduce saturation and scattering, depth sectioning techniques can be employed. In this regard, confocal microscopy is based on filtering out-of-focus light using a pinhole.[112,113] Optical coherence tomography (OCT) is an interferometric technique that was developed by Fujimoto's group[114] in 1991 and takes advantage of the short coherence length of a light source which allows to record coherence gated images and obtain µm-scale cross-sectional imaging of the target. OCT provides improved spatial resolution (1-10 µm) in scattering tissue, but with high acquisition times due to the point-wise (time-domain OCT) or line-wise (frequency-domain OCT)scanning mode, thus avoiding real-time imaging.[115–117]

Several studies reported the use of OCT imaging for tracking microagents in real-time. For instance, Li and co-workers employed a frequency-domain OCT setup to track magnetically-driven spherical microrobot (90 μm in diameter) *in vivo* in the portal vein of mice at a penetration depth of ~1.6 mm, with a line scanning rate of 5.5-70 kHz.[118] The same technique was also used to track reflective particles (polystyrene, 2 μm in diameter) as contrast agents to improve OCT imaging contrast in *ex vivo* mice liver and *in vivo* in zebrafish.[119] Likewise, SiO_2 particles (1.2 μm in diameter, half-coated with a thin film of Au) were functionalized with a specific antibody that recognizes a biomarker (cardiac troponin I) of acute myocardial infarction to perform on-chip nonspectroscopic optical immunosensing.[120] By using the same principle, Nelson's group tracked the position of a microrobot (size: 285×1800 μm) for minimally invasive intraocular surgery. The magnetic robots were steered using rotating magnetic fields in *ex vivo* porcine eyes as well as *in vivo* in lapin eyes and consecutive images were acquired at a speed of 15 Hz.[48] The same group implemented optical microscopy combined with an electromagnetic coil system (8 coils arranged in a hemispherical configuration) and proposed a cylindrical millimetric (1x0.5 mm) robotic system for vascular retinal surgery in an eye model (human-like model eye) with and without eye's lens (**Figure 5B, i-ii**).[121] An algorithm was proposed to localize the millimetric device based on its 3D structure. More recently, a similar concept was proposed to track magnetically driven micromotors employing IR light at a wavelength of 970 nm for performing *in-situ* microrheology analysis.[122] These reflective micromotors were successfully visualized with high spatial (about 20 μm) and temporal resolution (ms range) within scattering phantoms and *ex vivo* mouse skull tissues (**Figure 5C**). The reported penetration limit was 0.32 TMFP, corresponding to about 160 μm depth in real mouse skull tissues. The main limiting factor of the employed setup was the limited dynamic range of the camera. Strategies such as pulsed laser excitation, and the usage of wavelengths of the NIR-II optical window would improve the achievable penetration depth. While the discussed methods

suppress the scattered light, they result in a strong reduction of the SNR. In the Future Perspectives section, we will present methods that exploit the scattered light enabling increased SNR and penetration depth.

Fluorescence-based Imaging

FI is a widely used biomedical imaging modality; its working principle relies on the well-known Jablonski energy diagram[123] which describes the electronic energy states and the transitions between them. FI requires an excitation light source, a detector and image-forming optics to produce visual representation of the target object based on the distribution of fluorescent labels. Fluorescence or two-photon fluorescence microscopy[124] allows the reduction of background noise by using wavelength filters that suppress or at least reduce the contribution of the scattered light to the recorded signal. FI can have relatively low cost and produces no harm to living organisms if used in the IR range within the allowed exposure limits (typically 329 mW/cm^2 at 808 nm) indicated by the International Commission on Non-Ionizing Radiation Protection guidelines.[125] Fluorescence emission can be provided by specific labels or can be an intrinsic property of the materials (autofluorescence). Autofluorescence is the natural emission of light from structures upon light absorption. This is the case of proteins such as tyrosine and melanin, spirulina plant or non-biological polymer materials like photoresists. For instance, SU-8 photoresist shows an emission peak in the blue region of the spectrum (between 400-490 nm). This property, enable to track magnetic microrobots obtained from SU-8 doped with iron oxide powder in 2D open cell culture chambers while performing particle and cell manipulation.[126] Other examples of autofluorescent structures are the micromotors based on *Spirulina platensis* and are fabricated *via* dip-coating in a suspension of Fe_3O_4 NPs (**Figure 5D, i**). Such micromotors exhibited magnetic properties and biocompatibility due to their biogenic nature. The innate autofluorescence (emission at 660 nm) of the microalgae was achieved with an excitation wavelength of 552 nm, allowing the tracking of a

swarm of micromotors (ca. 10000 MRs with a typical length of single structure ~ 100 µm) *in vivo* with a spot size in the millimeter range (about 3-5 mm) and a temporal resolution of ~0.2 fps (**Figure 5D, ii**). This study was limited to subcutaneous tissues due to strong scattering of light at the specific emission wavelength.

To overcome this problem, the inclusion of fluorescent dyes that emit in the IR region (700-950 nm) have been proposed by the Nelson's group who reported *in vivo* studies of magnetically controlled microswimmers employing FI. They fabricated artificial bacterial flagella (ABFs) labelled with an isothiocyanate dye (NIR-797)[42] with an emission peak around 810-875 nm when excited at 745 nm and placed under rotating magnetic field (**Figure 5E, i**). A swarm of labelled magnetic ABFs (detection limit~15000 ABFs per ml) was tracked *in vivo* in the peritoneal cavity of a mouse when moving under rotating magnetic fields (9 mT, 90 Hz) with a temporal resolution of approx. 1 frame per second. (**Figure 5E, ii-iii**).

Standard fluorescent labels[127,128] have limitation issues associated with signal intensity strength, photobleaching, and short lifetimes.[129] Additionally, these fluorophores produce broad emission spectra that create overlapping detection ranges, making data analysis more challenging as highlighted by Nelson and coworkers.[42] To address these limitations, continuous development of species based on semiconductor nanocrystals have been carried out, in particular aimed at the development of a variety of quantum dots (QDs),[130] and more recently the upconversion nanoparticles,[131] that offer high sensitivity and penetration depths. There are few studies suggesting the use of QDs labelled MRs, for instance, MRs functionalized with toxic CdTe QDs were used as *in vitro* sensing platforms to determine the presence of Hg^{2+} and CH_3Hg^+,[132] and micromotors encapsulated with graphene QDs were used to detect deadly endotoxins released from *Escherichia coli* bacteria *in vitro*.[133]

FI has several advantages owing to its inherent properties: no ionizing radiation is required; high-resolution images are made at a high speed and this technique can be straightforwardly combined with other imaging modalities. Because fluorescent tags suffer the limitation of light penetration in biological tissues, it is a better choice to use this technique for MRs application in exposed organs such as the eye, or tongue, or near the skin. Another possibility is to look for NIR probes with longer wavelengths, meaning with reduced photon scattering and optical absorption (refer to the Future Perspectives section).

In summary, optical techniques offer excellent spatiotemporal resolution and molecular specificity that other techniques do not offer, a rich choice of contrast agents (dyes, QDs, and other fluorophores) or label-free approaches (reflection-based imaging) and high sensitivity which is extremely important for the tracking of MRs.

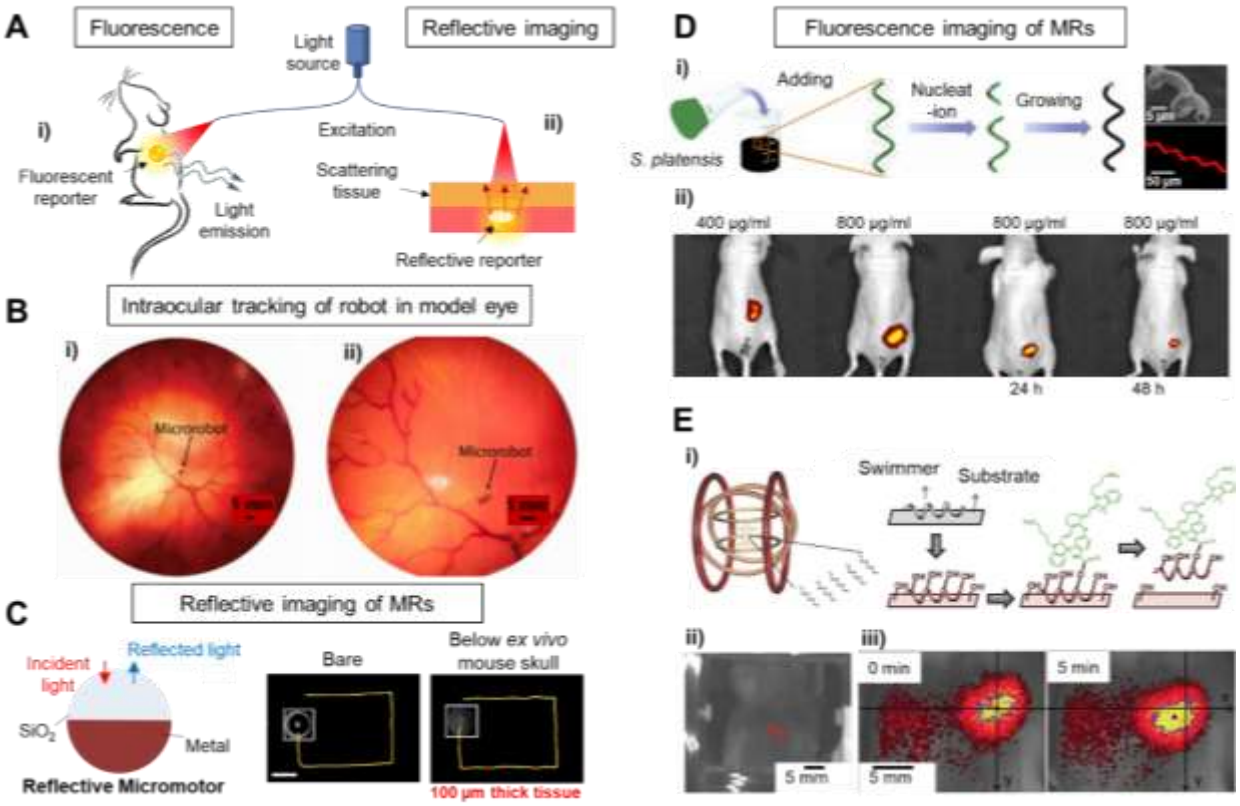

Figure 5. A) (i) Basic principle of fluorescence where light is emitted from target MRs upon excitation with incident light and (ii) reflection-based imaging where incident light is reflected back from the target micro-reflector. B) A cylindrical microrobot (1x0.5 mm) in an eye model (i) Intraocular environment through the eye's lens and (ii) without the eye's lens. Reprinted with permission.[121] Copyright IEEE (2012). C) Schematic of the reflective micromotor partially coated with metal layers and *ex vivo* tracking of single micromotors (100 μm in diameter) under mouse skull tissues (thickness from 80-110 μm). D) (i) Schematics of the dip-coating process of *Spirulina platensis* in a suspension of Fe_3O_4 NPs and (ii) fluorescence imaging of 100 μl of *Spirulina platensis*-72h with varied concentrations in the subcutaneous tissue of nude Balb/c athymic mice at three different time intervals. Adapted with permission.[43] Copyright AAAS (2015). and E) (i) Schematics of the *in vivo* experiment and functionalization process of ABFs with NIR-797 and optical microscopy images showing the controlled movement of ABFs *in vitro* and under rotating magnetic fields. (ii) The IR fluorescent image of the ABFs in a mouse. (iii) Fluorescent images

showing a swarm of ABFs swimming under the actuation of a rotating magnetic field. Adapted with permission.[42] Copyright Wiley (2015).

Ionizing Radiation-based Techniques

These techniques employ radiations in the high-frequency range of the electromagnetic spectrum (wavelength range: 100-10 nm). The employment of high energy radiation offers the advantages of high penetration depth and high spatial resolution yet could be harmful to human tissues if absorbed in excessive doses and for prolonged time. This set of techniques includes those based on X-rays and γ-rays which rely on radiation absorption or emission from the target, respectively. X-ray based imaging techniques remain the more consolidated ones in the field of medical imaging and range from traditional 2D radiography to fluoroscopy and 3D computed tomography. On the other hand, imaging techniques based on γ-rays such as PET and SPECT have been developed in the last decades of the 20th century and are more sophisticated in terms of molecular selectivity and spatial resolution, despite the abrupt cost of the associated equipment and the required imaging agents.

Although these techniques are well-established in the clinical practice, the employment of ionizing radiation-based techniques in the field of MRs tracking is still at its infancy and their application scenario should be carefully analyzed.

X-ray-CT Imaging

Radiography, fluoroscopy and computed tomography rely on the same electromagnetic radiations, namely X-rays (wavelengths in the range of 10– 10^{-3} nm). They differ essentially for the image acquisition timing, framerate and dimensionality, which is 2D in the first two cases and 3D in the latter.

The idea to use tomography in medical imaging dates back to 1895 when X-rays were discovered by W. C. Roentgen, but it took almost a century for the successful CT imaging device to be built.[134] X-rays are typically produced through a vacuum tube employing high voltage to accelerate electrons from a cathode to a tungsten alloy anode. During this acceleration process, the electrons release electromagnetic radiation in the form of X-rays. This kind of radiation transmits enough energy to ionize atoms and disrupt molecular bonds (also known as ionizing radiation). In general, such high energy allows high penetration depths, thus imaging of deep body regions. In X-rays imaging the sample is positioned between an emitter and a detector (**Figure 6A**). An image of the sample is reconstructed through the differences in radiation absorption across different materials: materials with high absorption coefficients cause a reduction in the radiation dose reaching the detector and appear visible in the produced radiograph. Materials with higher density (ρ) or high atomic number (Z) such as Gold, Iodine and Barium, feature higher X-ray absorption coefficient μ, defined as:

$$\mu = \frac{\rho Z^4}{AE^3} \tag{3}$$

where A is the atomic mass and E is the X-ray energy.

Among the human tissues, bones are typically well visible through X-rays due to the presence of Calcium. When imaging microrobots with X-rays, we could expect higher contrast with respect to the surrounding tissues for metallic structures while soft, polymeric or hydrogel-based microstructures are less trivial to visualize. However, contrast agents typically employed in the clinics and base on high atomic number compounds (*e.g.* Iodine) significantly enhance image contrast when embedded within the microrobot structure.

As anticipated, radiography enables to acquire only static 2D images of selected human body regions. More interesting scenarios for MRs imaging and tracking are opened by CT and fluoroscopy. In the first case, an X-ray source and opposite detectors are rotated around a workspace while 2D scans are taken at discrete angular increments over a complete 360° rotation. The projections are then processed to create a 3D reconstruction of the scanned object. The spatial resolution of CT imaging depends on the collimator dimensions, the number of detectors and the number of slices acquired over the 3D workspace. By decreasing the collimator size and increasing the number of detectors and 2D slices, a sub-millimetric resolution could be accomplished, accepting prolonged imaging time.[135]

Overall CT is not suitable for real-time applications if high spatial resolution is required. Safety reasons limit the exposure time of standard radiography as well with an impact on temporal resolution. On the other hand, Fluoroscopy differs from the other X-ray-based techniques as the images produced appear in real-time, allowing the evaluation of dynamic biological processes and guiding interventions. Electronic fluoroscopy systems develop this perception by capturing and displaying images at a high frame rate, typically 25 or 30 fps. At these frame rates, the human visual system cannot distinguish frame-to-frame variation and motion appears to be continuous, without visible flickers. To achieve high frame rates while reducing the cumulative radiation dose, the radiation dose to the image receptor per each frame must be kept quite low, about 0.1% of the dose used in radiography:[136] this limits the spatial resolution accomplished by the technique with respect to CT.

Although X-ray based imaging has been widely employed in the field of targeted therapy and microsurgery, *e.g.* for needle[137,138] or catheter steering[139] (fluoroscopy), the employment of these techniques in the field of microrobotics has been scarcely approached. Nguyen *et al.* proposed a real-time position and orientation tracking method for a millimeter-sized intravascular microrobot

based on the principal component analysis algorithm (**Figure 6B**). The suggested algorithm was implemented to control a wireless microrobotic system composed of a bullet-shaped object, a biplane X-ray imaging platform, and an electromagnetic actuation system. A tracking error below 0.4 mm was accomplished *in vitro* [140] (to be compared with the millimeter-scale of the microrobot). The same group demonstrated this approach on a pig to treat arterial thromboembolism through penetration of a blood clot by the microrobot. This was possible by combining remote magnetic control of the millirobot position and fluoroscopy.[141] Recently, Xu *et al.* exploited a full-field transmission X-ray microscope to actuate and image in real-time half-metal-coated Janus microparticles in aqueous solution. Both propulsion and visualization of the particles are activated by X-ray radiations.[142]

Overall, X-ray based techniques appear particularly interesting in terms of spatial and temporal resolution, potentially enabling real-time tracking and single microrobot/swarm imaging. However, side effects associated with excessive exposure to X-rays should always be considered. Nonetheless, it is worth underlining that, when properly balancing the exposure time, the X-ray energy and the frame rate (in the case of fluoroscopy), the delivered radiation dose can be acceptable with very low harm to body tissues.

PET-CT and SPECT Imaging

Nuclear imaging techniques rely on the detection of γ-rays (wavelengths lower than 0.1 nm). These radiations can be either emitted by radioisotopes, as in the case of Single Photon Emission Computed Tomography (SPECT) or generated upon positron-electron annihilation as in the case of Positron Emission Tomography (PET). The detection of the emitted γ-rays with tomographic techniques enables the 3D reconstruction of the distribution of γ-emitting compounds, thus the imaging of a target region. The γ-rays possess high energy and can penetrate deep across different kinds of medium, thus enabling deep tissue imaging in human-scale workspaces. However, nuclear

imaging itself provides poor information on morphological and anatomical features and call for the employment of specific tracers (*i.e.* imaging agents) able to emit γ-rays.[143]

PET and SPECT are minimally invasive high-resolution techniques which enable quantitative estimation of the number of radio-labeled species available in a specific location. Both techniques are widely employed in early diagnosis and in the evaluation of patient response to therapy by exploiting radiolabeled markers.[144] To these purposes, PET and SPECT are typically employed in conjunction with CT imaging to combine information on radioactivity distribution with anatomical ones.

The device for radiation detection is typically based on a scintillation camera which includes photomultiplier tubes to convert γ-ray photons into an electric signal. Radioactivity 3D distribution is assessed by combining projection images acquired through 360° rotations of the scintillation camera. The number and arrangement of employed detectors varies by technique, for instance assuming the sheet configuration in SPECT and the ring configuration in PET (**Figure 6A**). In the case of SPECT, a lead collimator is also required.

Specific γ -emitting compounds enabling nuclear imaging are typically based on lighter elements produced *via* cyclotron, such as ^{11}C, ^{13}N, and ^{18}F in the case of PET and on heavier elements such as ^{99m}Tc, and ^{123}I [145] with SPECT. PET radionuclides present very short half-lives ranging between ten minutes in ^{13}N and 110 minutes in^{18}F if compared with SPECT radionuclides ^{99m}Tc, and ^{123}I whose half-lives are 6 and 13 hours, respectively.

The γ-rays of PET generally possess higher energies and can travel through thicker tissues easily, experiencing lower attenuation compared to SPECT radiation. In addition, the production of two γ-ray beams in PET allows different detection modes (single incidence, true coincidences, *etc.*) leading to an increased sensitivity and spatial resolution. On the other hand, both positron emission

and annihilation must occur to produce γ-rays in PET, generating the risk of position estimation artifacts caused by the positron travel between the two events.[146]

Recently, some attempts to exploit nuclear imaging techniques to monitor and track MRs for medical applications have been reported. Sánchez and co-workers employed PET to track a large population of tubular Au/PEDOT/Pt micromotors (single tube length ~12 μm) in a tubular phantom. The absorption onto the micromotor surface of ^{124}I enabled PET tracking with 7 frames over 15 minutes. Results were confirmed by comparison with optical tracking, revealing the potential of such techniques towards *in vivo* microrobots tracking (**Figure 6C**).[147] Iacovacci *et al.* reported the use of SPECT imaging to localize soft hydrogel-based thermoresponsive microrobots and track their shape transition for controlled release of drugs in the target site. Imaging of single millirobot (3mm) in different configurations and across different dimensions was enabled by the inclusion in the hydrogel structure of ^{99m}Tc Zinc colloids. Results obtained with nuclear imaging were confirmed by comparison with CT images and with *ex vivo* study, where the millirobots were injected in the peritoneal cavity of a mouse [148] (**Figure 6D**). The works related to radiation-based imaging (PET and SPECT) of MRs are summarized in **Table 1.**

Overall, PET and SPECT offer great advantages with respect to other clinical imaging techniques especially in terms of penetration depth and selectivity (*i.e.* the ability to image specific elements). On the other hand, these techniques have bottlenecks related to large acquisition time preventing real-time imaging, to the high cost of the imaging apparatus and to the limited life-time of radio-emitting compounds. This makes these techniques more suitable for assessing an efficient target reaching and for post-operative monitoring than for fast position tracking. The radiation dose is also a critical point. However, when employing SPECT or PET for microrobots imaging, the absorbed radiation dose is significantly lower than the levels reached in X-ray CT. The reason is

that in CT an external X-ray source/detector arrangement performs a 360° rotation to irradiate all the body's anatomy, while in nuclear techniques the source of radiation is limited to the very small volume of the microrobots.

In conclusion, PET potentially offers better spatiotemporal resolution and image quality in comparison to SPECT, but high costs and very short half-life of employed radioisotopes limit their inclusion in MRs for durable targeted interventions. Nonetheless, this aspect can make PET better in terms of safety for other interventions.

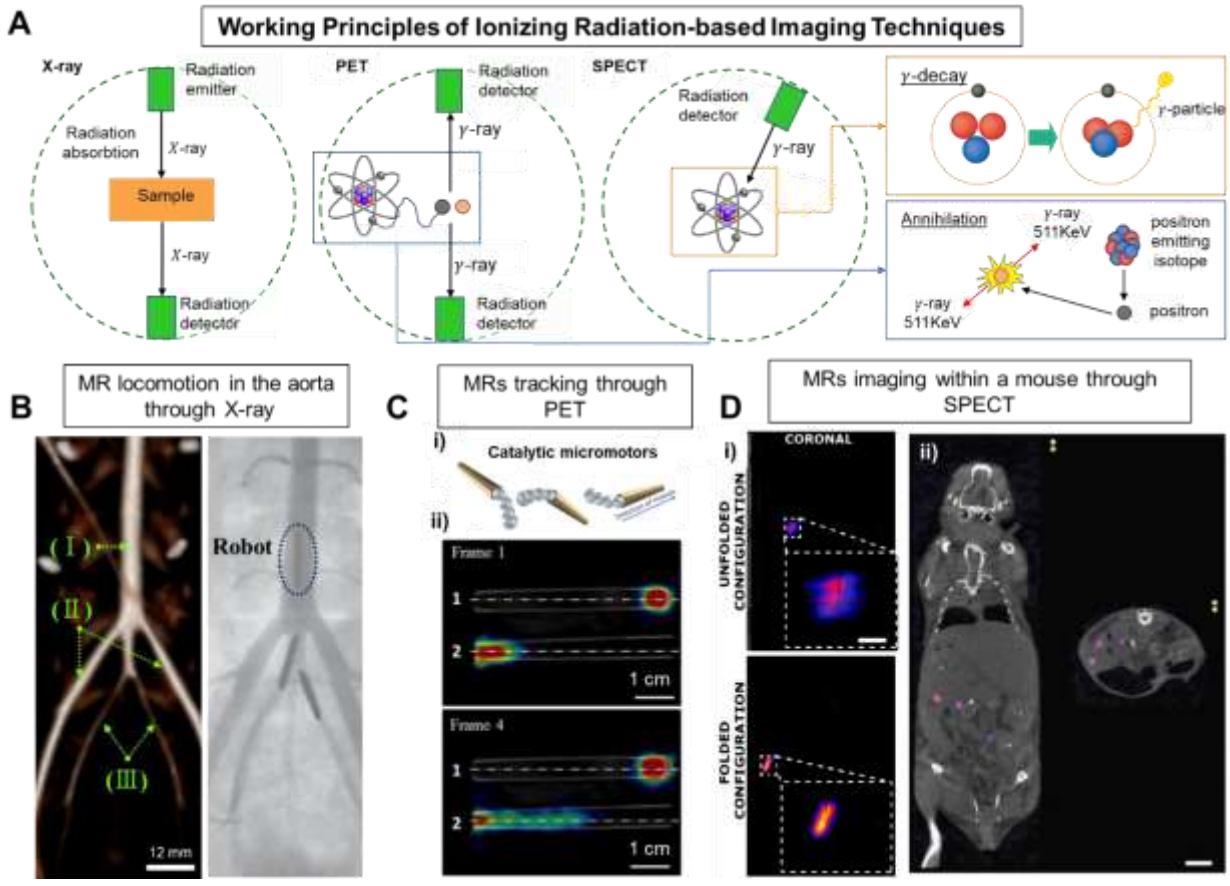

Figure 6. A) X-Ray, PET and SPECT working principle schematization with depiction of the γ-ray emission mechanisms and detector arrangements in the workspace. B) Locomotion of a microrobot from the abdominal aorta to the right/left external/internal iliac artery (I: Abdominal aorta, II: External iliac artery, III: Internal iliac artery). Reprinted with permission.[141] Copyright

Elsevier (2016). C) PET tracking of a swarm of catalytic Au-micromotors. (i) Schematic representation of the bubble propulsion mechanism of Au-micromotors. (ii) PET tracking of a swarm of micromotors in transparent tube phantoms. Adapted with permission from "Medical Imaging for the Tracking of Microrobots".[147] Copyright 2018 American Chemical Society. D) SPECT imaging of a soft magnetic hydrogel-based microrobot for drug delivery through shape switching. (i) Single microrobot imaging in the folded and unfolded configuration (scale bar 2 mm). (ii) *Ex vivo* imaging of multiple microrobots in the peritoneal cavity of a mouse (scale bar 10 mm). Adapted with permission.[149] Copyright Wiley (2019).

HYBRID IMAGING TECHNIQUES

Hybrid imaging techniques combine more than one physical principle to enable MRs higher detection within the region of interest. For example, photoacoustics takes benefit from both optical and US imaging. In particular images obtained by this technique have high contrast (due to the absorption of light), and high spatiotemporal resolution thanks the fact that US beam scatters ~3 orders of magnitude less as compared to photons.

Elsewise, magnetomotive MMUS exploits the detection of magnetically induced motions through the analysis of backscattered US waves. As a doppler-based technique, it does not involve the amplitude of backscattered waves, which enable enhanced contrast resolution. Furthermore, by controlling the characteristics of the magnetic excitation, it can be used to isolate specific motions in the FoV. This section will discuss the employment of the mentioned hybrid techniques to image and track MRs in biological tissues. In last section of this review, less explored hybrid concepts will be put into perspective to provide hints on their potential employment in the field of microrobotics.

Photoacoustic Imaging

PAI has emerged as a fast-developing medical imaging technique in the last decade[109,150–153] and was introduced by Alexander Graham Bell[154] in 1880 upon observation of the sound waves generated by the sunlight. PAI relies on the 'light-in, sound-out' approach: IR light penetrates the biological tissue and generates ultrasonic waves following the absorption of light. Short-pulsed or periodically modulated electromagnetic radiation is delivered with wide-field illumination and is absorbed by specific chromophores which cause localized and rapid increase in temperature and - in turn - US pressure waves. The contrast of PA images comes from the distribution of the absorbed optical energy and is thus related to the optical properties of the tissues and the wavelength of the incident light.[155] The sound waves generated from the optical absorbers are detected with US transducers and are reconstructed by using image generation algorithms.[156] Different US piezoelectric transducer geometries have been proposed: linear and cylindrical are used for two-dimensional imaging whereas spherical arrays allow the acquisition of 3D data set.[157,158] Typically a PAI system comprises a pulsed IR laser (600-900 nm and 1100-2000 nm, 1 to 100 ns pulse widths and 10-50 Hz pulse frequency), US transducer (256 or 512 elements) and on-board image reconstruction equipment as shown in **Figure 7A**.

PAI takes advantages of endogenous chromophores (*e.g.* lipids, melanin, hemoglobin) available in the body or exogenous contrast agents which absorb light at specific characteristic wavelengths[159,160] thus enabling their detection and identification with respect to the surrounding tissues and structures.[161,162] For instance, oxy- and deoxy-hemoglobin can provide anatomical functional information of vascular structures including blood oxygen saturation , flowrate and metabolism by employing multi-wavelength excitation.[150,163–165] PAI has the advantage of spectrally unmix the absorption spectra from diverse sources of absorption, thus enabling to discriminate structures and processes based on their composition or on the involved molecules. A

rich choice of exogenous contrast agents (dyes, NPs and reporter genes) can be used for molecular imaging. PA signals can be treated to extract both anatomical and functional features of tissue microenvironment. There have been several advancements in the PA reconstruction algorithms: deconvolution algorithms to retain the structural information,[166] filtered-back-projection algorithms,[167,168] and single-stage algorithms for high quality imaging[169] have been proposed depending on the intended application. The spatial resolution of PAI depends on the features of the US transducers, including the center frequency and the spacing between piezoelectric elements. Both the resolution and the imaging depth correlate with the US detection frequency, as well as, on the applied light wavelength and its pulse repetition rate. The spatial resolution of PAI ranges from several tens of micron (depth of a few mm) to sub-millimetre (depth of a few cm).[170]

PAI was suggested by part of us in 2017 as a promising tool to image single or few MRs in deep tissues and in real-time towards relevant biomedical applications.[47] Later on, part of the authors reported the use of PAI for real-time tracking of single magnetically-driven micromotors (100 µm in length) down to 1 cm depth in *ex vivo* chicken breast and phantoms.[171–173] The localization of distinct micro-objects was accomplished with an average error of ~100 µm in tissue-mimicking phantoms and 3D real-time positioning was also possible with this technique (**Figure 7B, i-iv)**. Moreover, by coating the micro-objects surface with gold nanorods (AuNRs) it was possible to enhance the contrast and the image quality thanks to the sharp and tunable absorption spectrum of AuNRs in the NIR region.

A follow-up work by Gao and co-workers[44] showed the real-time monitoring of drug-loaded capsules (between 70 and 750 µm in diameter) containing Mg-based particles (~20 µm in diameter) in living mice intestine using the same technique (**Figure 7C**, **i-iii**). The capsules were prepared with Au, a mixture of alginate and Doxorubicin, and parylene-C, all encapsulated in enteric

protective capsules (using the emulsion method)[174] to prevent reactions with gastric acids while passing through the stomach. After reaching the target site, continuous NIR irradiation (808 nm, 2W) induced disintegration of the protective capsules and doxorubicin release. Recently, multifunctional magnetized *Spirulina* microrobots (length: ~100 µm and swimmers count ~17520) coated with polydopamine (PDA) were imaged *in vivo* subcutaneously (~1.5 mm depth) (**Figure 7D, i**). Such PDA coated biocompatible MRs were aimed for fluorescence-based diagnosis and photothermal therapy of pathogenic bacterial infection.[46] The PA images were captured at an interval of 10 min to show the accumulation of PDA MRs under skin. Although PAI is promising for *in vivo* MRs tracking and offers higher penetration depth compared to pure optical techniques, it is still limited to 1 cm deep tissues while maintaining a spatial resolution about 100 µm in real-time. There is still a need to overcome the penetration depth limits imposed by light to enable MRs in human tissues (>5 cm deep) for any medical tasks.

In summary, PAI combines the advantages of light (high spatial resolution) with the penetration depth of US,[170,175] and spectral unmixing is a substantial feature to extract optical signatures of MRs from the surrounding tissues. It would be even advantageous to combine real-time US/PA with pre-acquired MR images towards more efficient diagnosis and therapy.[176] Another study highlights the dual-imaging system based on PAI and OCT for surgical guidance.[177] However, many applications require real-time imaging well beyond the penetration depths of PAI which is still challenging. Hybrid US and PA imaging (**Figure 7D, ii**) provides another interesting concept of functional and anatomical imaging, where US allows for accurate real-time tracking of MRs in deep tissues and PA is responsible for distinct signature discrimination from the surrounding tissues. In this regard, a submillimeter microrobot was imaged in opaque phantoms below 1.5 cm depth, with a spatial resolution of about 125 µm.[178] Recently, dual high-frequency US and PA imaging was used for the monitoring of swarms and single magnetically-driven spherical MRs (100

μm in diameter) in phantoms, *ex vivo* and *in vivo* (in mice bladder and uterus) intended for targeted drug delivery.[179] Furthermore, multi-wavelength excitation and spectral unmixing of injected MRs in tissue provided distinct spectrum signature compared to the tissue background after 3D reconstruction (**Figure 7D, iii**). The graph highlights the PA signal strength of the injected micromotors (yellow), oxy (red) and deoxygenated (blue) hemoglobin (**Figure 7D, iv**).

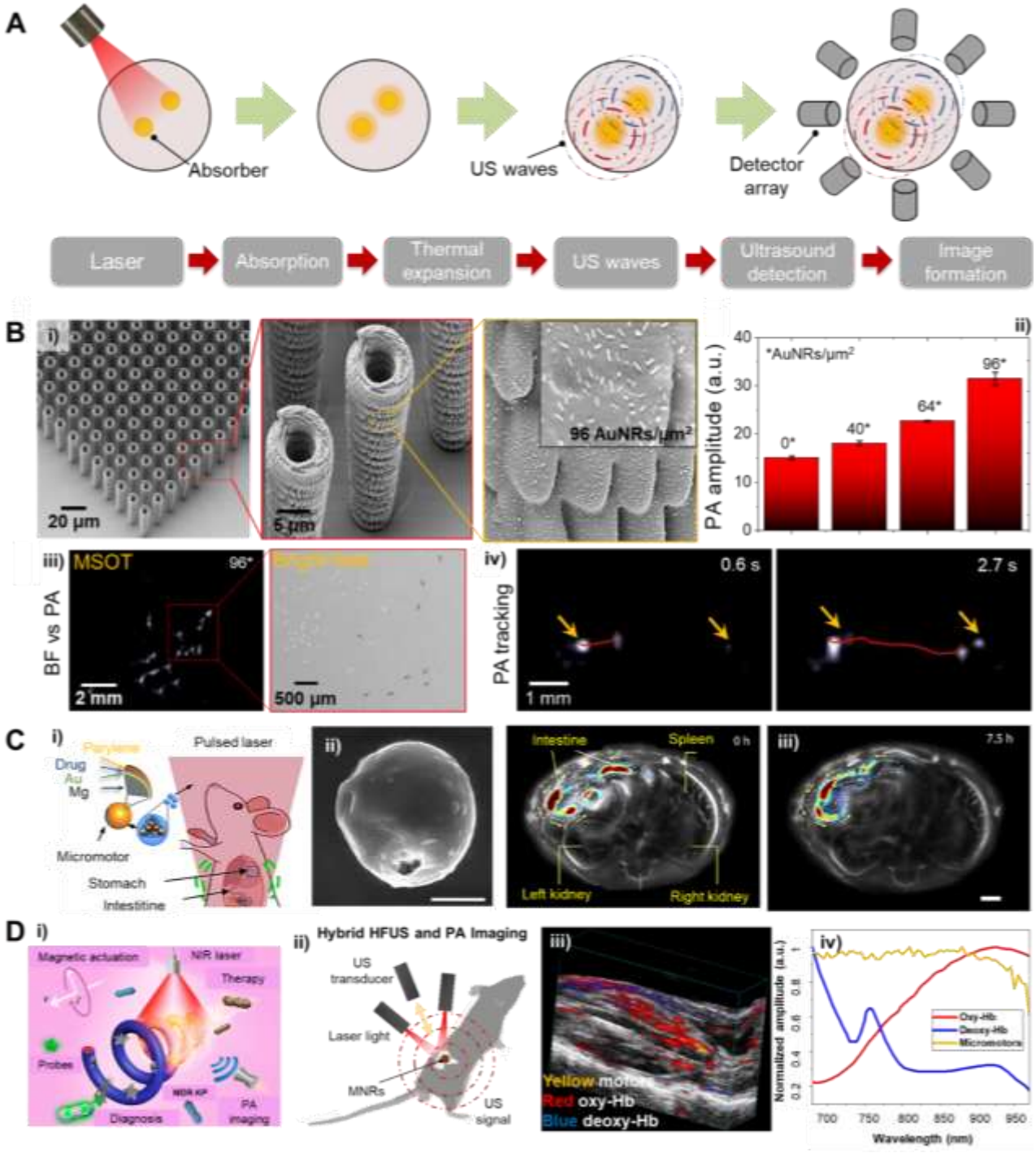

Figure 7. A) Working principle of photoacoustic imaging. When an absorber is exposed to a pulsed laser light, it absorbs light and undergoes thermoelastic expansion, thereby generating US signals which are then detected. B) (i) SEM images of an array of 3D printed micromotors before and after AuNRs functionalization. (ii) PA signals from micromotors (100 μm in length) sandwiched in

agarose phantoms (~1 cm depth) and with different density of AuNRs, (iii) PA signal of fully embedded micromotors with a density of 96 AuNRs/μm^2, and the corresponding bright-field image of the same sample, and (iv) Time-lapse images of a single 100 μm micromotor moving over a time period of 2.7 s. Yellow arrows show the static microstructures stuck on the phantom surface and red lines mark the trajectory of a single moving micromotor. Adapted with permission from "Real-time Optoacoustic Tracking of Single Moving Micro-objects in Deep Phantom and *Ex Vivo* Tissues".[171] Copyright 2019 American Chemical Society. C) (i) Schematic of the microrobotic system in the GI tract. The microcapsules are administered into the mouse GI track. NIR illumination facilitates the real-time PA imaging and subsequently triggers the propulsion of the micromotors in targeted areas of the GI tract. (ii) SEM image of an ingestible micromotor capsules. Scale bar, 10 μm. (iii) Time-lapse images of the capsules in intestines for 7.5 hours. The capsules migrating in the intestine are shown in color; the mouse tissues are shown in gray. Scale bar, 2 mm. Adapted with permission.[44] Copyright AAAS (2019). D) (i) Schematic illustrating the treatment of bacterial infection based on spirulina-functionalized micromotor. Adapted with permission from "Photoacoustic Imaging-Trackable Magnetic Microswimmers for Pathogenic Bacterial Infection Treatment".[46] Copyright 2020 American Chemical Society. D (ii) Schematic principle of hybrid high-frequency US and PA imaging. (iii) 3D reconstruction and spectral unmixing of injected micromotors in tissue. (iv) The graph highlights the PA signal strength of the injected micromotors (yellow), oxy (red) and deoxygenated (blue) hemoglobin. Adapted under American Chemical Society nonexclusive rights agreement for illustrations.[179]

Magnetomotive Ultrasound Imaging

MMUS is a US doppler-based imaging technique used to assess the presence of magnetic tracers (*e.g.* paramagnetic NPs) in the imaging area. The method was introduced by Oh and coworkers in

2006,[180] and has significantly evolved since then.[181–183] In MMUS, the imaging area is excited with time-varying magnetic fields while it is scanned with a standard pulse-echo US probe. Raw RF data, acquired by the ultrasound scanner, are processed by motion detection algorithms that are able to discriminate the regions where vibrations are induced by the exciting magnetic field, *i.e.* the regions perfused with the magnetic tracer (**Figure 8A**). Different algorithms have been proposed in the past decade to detect magnetically induced motions. All the solutions are based on acoustic signal phase-shifts evaluation, with shifts produced by magnetic tracers movement. Popular approaches for motion detection include time-domain cross-correlation methods,[184] frequency-locked methods,[185] and blind source separation methods.[186]

Being a US based technique, MMUS provides not only a measure of the presence of magnetic material in the imaging area, but also anatomical and morphological information regarding tissues. It is commonly used in elastography applications and for molecular imaging purposes. In fact, MMUS can be used to assess mechanical and chemical properties of tissues perfused with NPs, through the analysis of magnetically induced motions. In 2017, Evertsson and coworkers used MMUS, in combination with PET/CT imaging, for clinical assessment of a sentinel lymph node (SLN) rat model.[183] Paramagnetic NPs (40 nm in diameter) were injected in the peritumoral region and accumulated in the SLN. Particle's motions, hundreds of nanometers in amplitude, were induced by an external electromagnet and detected with a high-resolution US probe (32 MHz). The reconstructed distribution of NPs motions provided information regarding the shape and the stiffness of the SLN (**Figure 8B**).

In contrast to MPI, in MMUS the signal detected from the tracers motion does not allow to quantitatively estimate their distribution in the FoV. The reason is that NPs motion depends not only on magnetic quantities (*e.g.* magnetization curve, magnetic excitation signal) which are

known, but also on the concentration of NPs that effectively accumulate in the site and on the viscoelastic properties of the surrounding medium which are usually unknown. Current research is aiming at developing MMUS algorithms for quantitative assessment of NPs distribution (known as the inverse MMUS problem) by comparison of MMUS images with offline simulated models (**Figure 8C**).[187]

Assessing the spatial resolution of MMUS is not straightforward. On one hand, the pixel size of a MMUS image is the same as in a standard B-mode image. On the other hand acoustic phase-shifts analysis enables to detected motions also in the nanometer range.[188,189] In this sense, this technique could be suitable also for nanoscale objects detection.

Temporal resolution is one of the bottlenecks of this technique. Currently available MMUS platforms require several US frames (called ensembles) to elaborate a MMUS image with acceptable SNR. Common algorithms running on standard platforms require an ensemble at least 5 s long to elaborate a clear MMUS image.[190] Different groups are currently investigating solutions for improving temporal resolution of MMUS imaging.[191–193]

Overall, this technique provides the ability to detect motion events down to the nanometer scale. Although currently used for characterizing tissues in quasi-static conditions, it can be potentially exploited for dynamic tracking of moving MRs, as for examples swarms in dynamic equilibrium. However, more research efforts are needed to obtain better performances in terms of temporal resolution and to progress towards real-time monitoring. Future studies shall also address the robustness of this technique to physiological and biological motions in clinically relevant scenarios (*e.g.* due to breathing and hearth beating).[194]

The works related to hybrid imaging (PAI and MMUS) of MRs are summarized in **Table 1.**

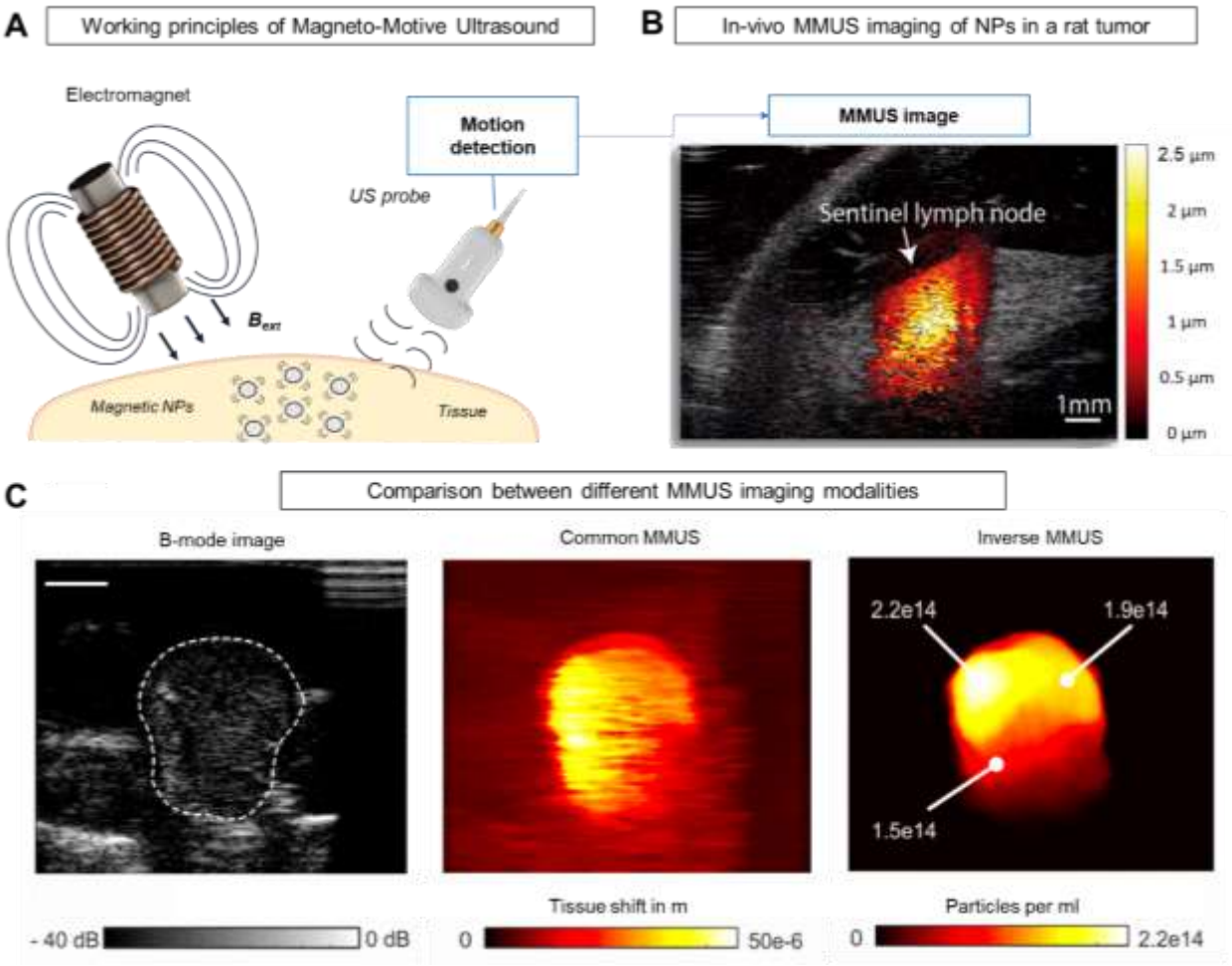

Figure 8. A) Working principle of MMUS imaging. Motions of magnetic NPs are induced by external magnetic fields and detected by an US probe. B) *In vivo* MMUS image of NPs (~20-100nm diameter) induced motions within a sentinel Lymph node in a rat model. Reprinted in part with permission under a Creative Commons CC-BY License from "Combined Magnetomotive Ultrasound, PET/CT, and MR Imaging of 68Ga-labelled Superparamagnetic Iron Oxide Nanoparticles in Rat Sentinel Lymph Nodes *In Vivo*".[183] Copyright 2017 Springer Nature. C) Comparison between standard B-mode, Common MMUS and Inverse MMUS images of a NPs distribution in phantom. Scale bar is 5 mm. Reprinted with permission under a Creative Commons CC-BY License from "Quantitative Imaging of the Iron-Oxide Nanoparticles Concentration for

Magnetic Drug Targeting Employing Inverse Magnetomotive Ultrasound".[187] Copyright 2019 De Gruyter.

DISCUSSION

The selection of the most suitable imaging technique depends on various factors ranging from the target application to the features of the microrobot. In particular, while looking for the best imaging strategy, it is important to consider: (*i*) system dynamics, namely either the need to perform real-time point-to-point tracking or time-discrete monitoring; (*ii*) MRs locomotion strategy and compatibility between actuation and imaging stimuli; (*iii*) dimension of the single microrobot and possible presence of a swarm; (*iv*) operating working district; and *(v)* duration of the MR-assisted intervention. Selecting the best imaging strategy while fulfilling a good compromise between technological and clinical specifications is not straightforward. The analysis of the state-of-the-art reported in the previous sections revealed that no single imaging technique can solve current medical microrobotics challenges and that each imaging modality has its own strengths and limitations.

The X-rays feature high resolution and deep penetration in body tissues but require expensive instrumentation. Furthermore, potential ionization can eventually cause damage to the medical personnel/patient, calling for the need of tuning radiation dose and exposure time. On the other hand, optical imaging methods based on fluorescence or reflection are somehow safe and carry high spatial resolution but have reduced tissue penetration which limits their application to sub-skin/superficial levels. MRI enables deep tissue imaging without any contrast agent along with acceptable spatial and temporal resolution but requires strong magnetic fields and expensive infrastructure. US alone suffers from spatial resolution but provide real-time monitoring and deep

tissue penetration together with low cost and high safety. **Table 1** summarizes the main results and performances obtained with conventional and hybrid imaging techniques in the field of microrobotics while underlying their employment in imaging/tracking a single or swarm of MRs *in vitro*, *ex vivo* or *in vivo* conditions. As underlined in the previous sections, most of the MRs imaging and tracking works reported till now have demonstrated the potentialities of medical imaging in MRs tracking and localization mainly *in vitro* or in tissue-mimicking phantoms. Just a few demonstrations combining *in vivo* localization and closed-loop imaging assisted position control have been reported.[42–46] This state of the art reflects that, despite the potentialities, huge engineering efforts are still needed to progress towards clinic. Interesting perspectives are envisioned by hybrid techniques and multimodal imaging, which allow to combine the strength of different techniques and overcome their limitations by exploiting multiple physical principles. Not surprisingly, most of the reported *in vivo* MRs tracking works combined more than a single imaging technique (*e.g.* MRI+FI, PAI+US, US+FI, *etc.*).

While addressing future research in this field, it is worth considering that swarm control somehow smooths the technical requirements needed for MRs imaging. In real clinical settings and therapeutic paradigms, probably MRs swarm or larger carriers transporting multiple cells will be likely employed to effectively deliver the required therapy to the target region. Due to their increased spot size, swarms of MRs relax the requirements for high spatial resolution. In addition, swarms can potentially enhance the contrast between MRs and soft tissue and enable a more robust localization within the body. In fact, tissue intrinsic contrast and physiological motions (*e.g.* breathing, heart beating) pose an additional challenge in tracking moving MRs *in vivo*, which calls for the development of efficient contrast mechanisms to equip the MRs with. This considered, swarm control appears as a promising strategy due to enhanced contrast to some imaging

techniques (*e.g.* US-based, like B-mode, Doppler, MMUS), and for the easiness of embedding higher doses of the contrast agent within the swarm formations.

Table 1. Summary of all imaging techniques for medical tracking of MRs

Magnetic field based								
Micromotor type/propulsion	**Label**	**Feature size**	**Tracking speed**	**Penetration depth**	**Biocompatibility**	**Complexity**	**Ref.**	**Comments**
Spirulina / magnetic propulsion and guidance	Fe_3O_4 NPs	10000 spirulina structures (spot size: 3-5 mm; element size: ~100 µm)	1 frame / 7 min	***In vivo*** (Mouse intragastric injection)	+++	-	Yan *et al.* 2018[43]	**MRI** Good spatial resolution Tissue imaging High penetration depth Expensive infrastructure
Magnetotactic bacteria / bacteria propulsion, chemotactic and magnetic guidance	/	Swarm of bacteria (element size: ~2 µm)	-	***In vivo*** (tumor injected in the left flank of a mice)	+++	-	Felfoul *et al.* 2016[64]	
Helical propeller /magnetic propulsion and guidance	Fe_3O_4 NPs	4x2 mm elliptical	10 fps	***In vitro*** (3x3cm arena)	+	-	Bakenecker *et al.*[75]	**MPI** Fast actuation and imaging Limited FOV Poor spatial resolution
Dispersed nanoparticles /magnetic propulsion and guidance	Fe_3O_4 NPs	6x3 mm elliptical	0.5 fps	**In Phantom** (bifurcated vessel)	+++	-	Griese *et al.* 2020 [76]	
Ultrasound based								
Spherical microparticle / magnetic propulsion and guidance	/	100 µm	Real-time (fps>100 Hz)	***In vitro*** (2x2 cm arena with aqueous solution)	+++	+	Khalil *et al.* 2014[83]	**B-mode** Real-time Cheap Tissue imaging Poor spatial resolution and contrast
Tumbling microrobot / magnetic propulsion and guidance	/	800 µm	Real-time (fps>100 Hz)	***Ex vivo*** (<1cm, dissected colon)	+	+	Bi *et al.* 2019 [88]	
Colloidal swarm of nanoparticles / magnetic propulsion and guidance	O_2 bubbles	Swarm (spot size, ~800 µm; element size, 500nm diameter)	Real-time (fps>100 Hz)	***Ex vivo*** (<1cm, bovine eyeball)	++	++	Yu *et al.* 2019 [94]	
Suspension of hollow silica nanoshells / not propelled	Gas-filled silica shells	Swarm (spot size, ~3 mm; element size, ~400 nm diameter)	Real-time (fps>100 Hz)	***In vivo*** (2 cm, rabbit)	+++	++	Liberman *et al.* 2016 [97]	**Doppler** Good contrast

								Limited lifespan
Optical based								
Magnetic Helices / magnetic propulsion and guidance	NIR-797 dye	Swarm (80000 ABFs; element size, ~16µm)	1 frame/ 1 min	***In vivo*** Mouse peritonial cavity	+	++	Servant *et al.* 2015[42]	**Fluorescence** Good sensitivity Poor spatial and temporal resolution
Spirulina/ magnetic propulsion and guidance	Autofluorescent	Swarm (10000 structures; element size, ~100µm)	1 frame/ 5 min	***In vivo*** Mouse subcutaneously	+++	++	Yan *et al.* 2018[43]	
Reflective particles / magnetic propulsion and guidance	Metal layer	20 µm	Real-time (30 fps)	***Ex vivo*** 160 µm deep mouse skull	+	+++	Aziz *et al.* 2019[122]	**Reflection** High spatio-temporal resolution Poor penetration depth
Radiation based								
Janus particle / X-ray propulsion	/	6 µm	Real time	**In Phantom** (chamber with water and glycerol)	**---**	++	Xu *et al.* 2019[142]	**X-rays** High penetration depth High resolution Tissue imaging Hazardous Expensive
Bullet-shaped microrobots / magnetic propulsion and guidance	/	2 mm (diameter) – 15 mm (length)	Real.time	***In vivo* (living pig blood vessels)**	**+**	**-**	Jeong *et al.* 2016[141]	
Catalytic / chemical propulsion and magnetic guidance	Iodine isotope	Swarm (10-20 structures; element size: 10µm)	7 frames / 15 min	**In Phantom** (tube containing turbid solution)	---	++	Vilela *et al.* 2018[147]	**PET-CT** High resolution High penetration depth Hazardous Low speed
Tubular microrobots / not propelled	^{99m}Tc Zinc colloids	100-500 µm	static	***Ex vivo*** (mice subcutaneous injection)	**+++**	**++**	Iacovacci *et al.* 2019[148]	**SPECT** High resolution High penetration depth Poor temporal resolution
Hybrid techniques								

Magnetic microtubes / magnetic propulsion and guidance	AuNRs	Single (100 µm in length)	Real-time (10 fps)	***Ex vivo*** (~1 cm deep)	++	+	Aziz *et al.* 2019[17]1	**PAI** Real-time Molecular information Improved resolution and penetration depth
Microcapsules / not propelled	Mg/Au/ Parylene	Swarm (100 µm)	Real-time (fps~2Hz)	***In vivo*** (~1 cm deep *in vivo*, mouse stomach)	+++	+	Wu *et al.* 2019[44]	
Spiruline micromotors / magnetic propulsion and guidance	Polydopamine (PDA) +Fe_3O_4 NPs	Swarm (spiruline concentration of min. 25 µg/mL) Spiruline size (>100µm, diameter ca. 10 µm)	1 frame/ 10 min	***In vivo*** (mouse subcutaneous infection model)	+++	+	Xie *et al.* 2020[46]	
Suspension of paramagnetic nanoparticles / not propelled	Fe_3O_4 NPs	Swarm (NPs concentration of 1-4 mgFe/mL) NPs size (40 nm diameter)	0.3 fps	***In vivo*** (mouse subcutaneous infection model)	+++	+	Everts son *et al.* 2017[183]	**MMUS** Improved contrast and spatial resolution Poor temporal resolution
Magnetic microparticles / magnetic propulsion and guidance	/	Single and swarm (100 µm in diameter)	Real-time PA (5-20 fps)	***In vivo*** (mouse bladder and uterus)	++	+	Aziz *et al.* 2020[179]	**Dual US/PA** Anatomical and functional imaging

(+++) represent the highest safety level/low complexity and (---) represent lowest safety level/high complexity

FUTURE PERSPECTIVES

As highlighted in the previous sections, there is no "hero" imaging technique that can outperform all the others. Instead, cleverly designed hybrid imaging techniques and innovative labels are being explored to move the technological boarders towards exciting application areas. Such perspectives will be analyzed in the following paragraphs.

Contrast Enhancing Labels

One of the big difficulties and challenges for *in vivo* MRs applications is performing non-invasive, real-time, deep-tissue, high-resolution and three-dimensional imaging. Scientists are currently working to improve several imaging techniques that could be applied based on their performances and working principle for MRs tracking. This section will mainly focus on how the employment of suitable contrast agents can significantly enhance imaging quality. Some of the limitations of

current imaging techniques for the tracking of MRs can be mitigated by incorporating suitable contrast agents varying by imaging modality as highlighted in **Table 2.** A multi-modal MR is also proposed embedding frontier contrast mechanism for multifunctional medical MRs **(Figure 9**).

MRI relies on contrast mechanisms to enlarge the difference in the relaxation times between different objects and its specificity may be improved through the development of relevant contrast agents. Current research is investigating the potentialities of MRI contrast mechanisms based on Quadrupole Relaxation Enhancement (QRE). Specifically, the interaction between water protons and suitable quadrupolar nuclei can lead to QRE of proton spins (provided the resonance condition between both spin transitions is fulfilled[195]). This effect could be utilized as a frequency selective mechanism in T1 shortening contrast agents for MRI. Theoretically, the contrast enhancement factors of QRE are smaller than those of typical paramagnetic contrast agents. However, this mechanism depends on the characteristics of the applied external flux density, a property that can be exploited to enhance the relative contrast of properly designed materials with special field-cycling MRI scanners.[196] So far, QRE has been observed for solids (in most cases for ^{14}N) as a result of very slow dynamics and anisotropic spin interactions, believed to be necessary for QRE to appear. However, a recent study has shown the evidence that QRE can be achieved in solutions containing a high spin nucleus (209Bi) as the quadrupole element, for the exploration of QRE in biomedical MRI and perhaps in MRs imaging and tracking.[197]

Concerning MPI, suited contrast agents exhibiting very steep magnetization curves may be explored to further increase spatial resolution. It has been demonstrated that increasing the NP core size improves the magnetic susceptibility (steepness of magnetization curve) and leads to higher spatial resolution. However, this effect is limited by the so-called relaxation wall (25 nm core diameter), which causes blurring in images due to relaxation losses.[198] Recent studies highlighted

that low-amplitude and low-frequency drive field parameters help mitigating relaxation losses.[199] A combination of larger NP core sizes and optimized drive field parameters may lead to the development of improved contrast agents, allowing to enhance MPI spatial resolution and make a considerable step towards MR tracking and control applications.

US imaging offers real-time monitoring and deep tissue penetration but lacks in high spatial resolution. To improve this, future research should focus on functionalizing MRs with suitable contrast agents,[200] *e.g.* microbubbles and/or gas vesicles, to discriminate them from the surrounding environment. Promising results in this direction were reported in a recent Nature paper.[201] Clusters of micro-organisms (cells, bacteria, vesicles), at 0.1% volumetric concentrations, were labelled with acoustic reporter genes and visualized *in vivo* in mammalian hosts with a resolution of 100 µm. Moreover, the use of high-efficiency US contrast agent may also enable advancements in super-resolution US through ULM, bringing such techniques one step forward in real-time imaging. US contrast agents may also be beneficial for hybrid US-based techniques. A recent study demonstrated that MMUS contrast and sensitivity can be significantly improved through the use of SPIO labeled microbubbles (SPIO-MBs).[202]

Concerning optical imaging, conventional IR imaging (FI and RI) uses the first biological window with a wavelength range from 700 to 950 nm (NIR-I), and recent advances suggest the use of the second biological window (NIR-II, 1000-1400 nm) for deeper tissue penetration, reduced autofluorescence, minimum photon scattering and better SNR.[110,203] Almost 16 years ago, simulations suggested it would be possible to improve SNR by 100-fold using fluorophores with emission peaks at around 1320 nm (NIR-II).[204] Since then, there was not much progress due to the lack of biocompatible fluorescent labels in that range. Early reports were mainly focused on II-VI (CdTe and HgTe),[205] IV-VI (PbS and PbSe)[206] and III-V (InAs)[207] QDs. However, the intrinsic

toxic nature of Pb, Cd, and As made them unfit for prolonged *in vivo* applications. A recent class of biocompatible QDs, I-VI (Ag_2S and Ag_2Se) emitting in NIR-II is demonstrated as a promising fluorescent probe.[208,209] Such QDs show good biocompatibility, high performance and no substantial toxicity. MRs labelled with these QDs, can emit light in NIR-II and act as an asset for future deep tissue *in vivo* FI.

PAI is suitable to distinguish target MRs from the surrounding tissues and is mainly utilizing conventional NIR-I window. One possibility is to shift the excitation light from traditional NIR-I to NIR-II window for deeper tissue penetration and improved contrast. Second, PA contrast agents are mostly composed of inorganic materials and the development of organic NIR-II agents can provide improved performance for deep *in vivo* imaging of MRs. An excellent PA contrast agent should possess NIR-II absorption peak, good photostability, high-molar extinction coefficient, low toxicity, high target affinity and biocompatibility.[210]

High atomic number elements play a major role in ionizing radiation-based techniques. Radioisotopes are fundamental imaging agents for PET and SPECT. The possibility to produce radiocompounds with specific chemical properties enables better inclusion of the imaging agents in the MRs structure and higher stability. Furthermore, as commonly done in the clinical practice, the possibility to functionalize such radiotracers to enable the binding with specific ligands so as to perform target-specific imaging, suggests a wide plateau of possibilities in the field of MR mediated targeted theranostics.[211–213] Elsewise, NPs made from high atomic number elements such as gold, bismuth, ytterbium and tantalum can be employed as x-ray contrast agents to improve the spatial resolution of these techniques. In fact, it has been demonstrated that such NPs provide better imaging properties, longer blood circulation times and lower toxicity than conventional iodinated X-ray contrast agents.[214] Additionally, the combination of two or more of these elements into a

single carrier allows for the development of multimodal and hybrid contrast agents, for instance exhibiting optimal contrast properties over a range of different X-ray tube potentials or being suitable for more than one imaging modality (*e.g.* combination of X-ray and MRI). A good perspective is also represented by the potential translation of X-ray luminescent (XL) and X-ray fluorescence (XF) into biomedical imaging domain. These computed tomography techniques use external X-rays to stimulate secondary emissions (either light or secondary X-rays). These modalities surpass the limits of sensitivity in current X-ray imaging and promise to break through the spatial resolution limits of other *in vivo* molecular imaging modalities.[215] Smart materials can be investigated to explore the use of these phenomena in microrobotics applications.

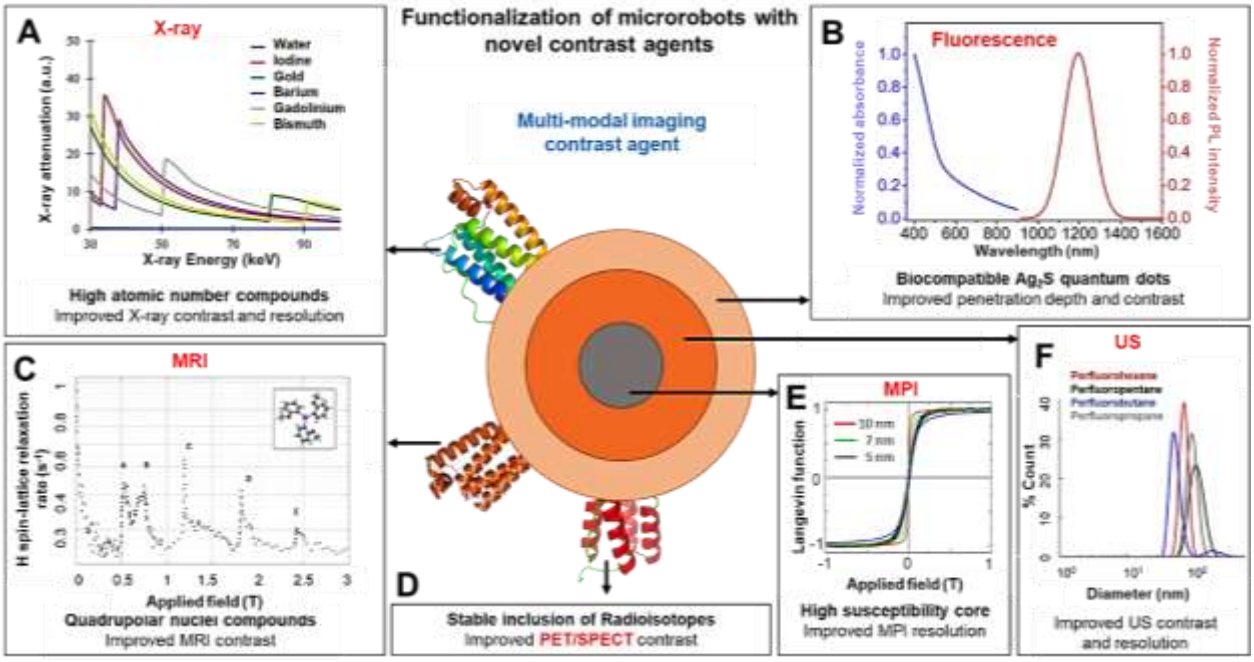

Figure 9. Suitable contrast agents for functionalizing medical MRs. A) Improved X-ray attenuation characteristics of high atomic number elements. Reprinted in part with permission under a Creative Commons CC-BY License from "*In Vivo* Small Animal Micro-CT using Nanoparticle Contrast Agents".[216] Copyright 2015 Ashton. B) Emission (NIR-II window) of biocompatible QDs. Reprinted in part with permission.[217] Copyright Elsevier (2014). C) Frequency-dependent

relaxation rate of quadrupolar nuclei for QRE. Reprinted with permission under a Creative Commons CC-BY License from "Tuning Nuclear Quadrupole Resonance: A Novel Approach for the Design of Frequency-Selective MRI Contrast Agents".[196] Copyright 2018 American Physical Society. D) Stable inclusion of radiocompounds for nuclear imaging contrast. E) Steeper magnetization characteristics of larger superparamagnetic cores. Reprinted in part with permission under a Creative Commons CC-BY License from "Solvent-Surface Interactions Control the Phase Structure in Laser-Generated Iron-Gold Core-shell Nanoparticles".[218] Copyright 2016 Springer Nature. F) Size distribution of US contrast agents measured using dynamic light scattering. Such agents can be labelled with MR for improved contrast. Reprinted in part with permission from "Spontaneous Nucleation of Stable Perfluorocarbon Emulsions for Ultrasound Contrast Agents".[200] Copyright 2019 American Chemical Society.

Table 2. Contrast enhancing labels for MRs

Imaging technique	Detection signal	Suitable Label/Materials	Binding mechanism	Comments	Ref.
MRI	RF waves (emitted by spin relaxation)	Quadrupolar nuclei for spin relaxation enhancement Iron oxides Metal alloys	NA	Contrast mechanism depends on the applied external flux density	196
MPI	Harmonics from magnetization saturation	Paramagnetic NPs with higher core size	NA	Effect limited by the relaxation wall	198
US	Backscattered US waves	Gas-filled bubbles/vesicles/shells (either collapsing or resonant)	Covalent binding of microbubbles with MRs surface	Improve contrast and sensitivity and enable super-resolution imaging. Disadvantage is their limited life-time (from several seconds to few minutes *in vivo*)	97,101,201
Optical-based	Fluorescence (confocal configuration)	QDs in NIR-II Organic dyes Fluorescent proteins Upconversion materials	Covalent binding Electrostatic interaction and self-assembly	Label MRs with Ag_2S QDs in NIR-II (1-1.4 μm)	42,133,219
	Reflection signal from robots	Reflective materials like Au, Ti	NA	Au and Ti are biocompatible	122

X-ray	Transmitted x-ray beam	High atomic number elements (*e.g.* gold, bismuth, ytterbium, tantalum) nanoparticles	NA	Improved spatial resolution, longer blood circulation times and lower toxicity	[214]
SPECT/PET	Emitted γ-ray beam (by radiocompounds)	Radioisotopes	Chemisorption	Radiocompounds with specific chemical properties enable better inclusion in the MRs structure and higher stability.	[211–213]
Photoacoustic imaging	US detection of acoustic waves generated by labelled AuNRs	Nanoparticles Molecular NIR dyes Absorbing metals Endogenous absorbers	Covalent (carboxyl groups	As a prominent example, Au nanorods functionalized onto the MR enhance the PA signal and provide a distinct signature to be discriminated from tissues	[171]
MMUS	US detection of magnetically induced motions	SPIO-labeled microbubbles	NA	Improved contrast and sensitivity	[202]
Hybrid US and PA	US detection of graphene microbubbles	Dual imaging mode graphene-based microbubbles for both US and PA imaging	Can be covalent bonding	There are few studies regarding the dual imaging contrast agents	[220]

*NA - not applicable

Recent trends in Hybrid Imaging

Modern imaging techniques that take advantage of different physical principles to gain in both spatial resolution and penetration depths are nowadays in the pre-clinical stage (*e.g.* PAI,). These hybrid techniques seem promising for testing MRs *in vivo* while controlling their motion and therapeutic tasks performance. Scientists from different disciplines are working on manipulating light, sound, and magnetic fields to overcome the diffraction and scattering limitations of current techniques. This can be possible by employing hybrid techniques or by functionalizing the MRs with absorbers, emitters or reflectors to enable improved sensitivity and contrast. In the following, innovative and promising hybrid techniques will be described to provide useful hints to the field of micro- and nanorobotics. **Figure 10** shows basic principle and schematic illustration of such imaging concepts.

Acousto-Optic Imaging

Acousto-optic imaging (AOI)[221,222] does not require any optical absorption (differently from PAI) but is based on the acousto-optic effect.[223] US waves when propagating through an illuminated area, induce changes in the tissue refractive index and in the scatterers position, resulting in the formation of side-bands in scattered light (**Figure 10A**). The number of photons contained within these side-bands are also called tagged photons and provide information on the light-intensity through localized acoustic focus spot. The AOI concept was proposed by François Micheron and Daniel Dolphi in 1989. The technique employs a focused US beam to modulate light inside the target area. Focused US is generated by an external transducer and the modulated light from the target is recorded outside the sample using interferometry-based approaches[222] thus enabling the reconstruction of light intensity crossing the sample. AOI directly maps the light irradiance being also sensitive to scattering properties of tissues. However, the spatial resolution is limited by the US focus spot, being from several hundreds of μm to mm range at depths of few cm in tissue. Typically, focused US beam (MHz range) in combination with NIR light or pulses (ns range) are used. The most challenging issue with this technique lies in the detection and quantification of tagged photons, and this technical obstacle still places AOI in the level of a proof of concept technique. One should address this challenge before implementing AOI for imaging MRs and one possibility could be to integrate the wavefront shaping method with AO setup for improved detection of wavefronts (tagged photons) in deep tissue.

Magneto-Optic Imaging

Magneto-optic imaging (MOI) is another hybrid imaging technique that combines an electromagnetic effect (eddy current or magnetic flux leakage) and the Faraday effect to generate a two-dimensional image. This technique was proposed and developed in the 1990s.[224] The propagation of light through a magnetic field is used to image target objects (*e.g.* defects or cracks

in the surface of an object). A pulse generator sends an alternating current to the excitation coil which induces eddy currents in the sample. These eddy currents induce in turn magnetic fields when encountering any defect or damage in the sample surface. If the sample is illuminated by polarized light, the defect-induced magnetic field modulates the polarized light that now contains the information on the magnetic field distribution, which correlates to the surface defect. The reflected polarized light is captured by a CCD or CMOS camera to form a 2D real-time image of the target (**Figure 10B**).

Until now MOI has applications in detecting surface defects or cracks and corrosion in aircraft skins for testing purposes.[225] By using a pair of polarizers one can visualize and quantify the field distribution across the sample surface and by detecting the stray magnetic fields the magnetic properties of the materials can be detected. The MOI technique was mainly dedicated to identify defects/cracks in thin films.[226] By taking advantage of this, the MRs can be designed with small cracks/defects during the fabrication process using various lithography techniques (*e.g.* photolithography, 3D lithography, e-beam lithography or stamp printers). Of course, limitations imposed by light penetration have to be considered to verify the feasibility of this approach in a target district. Future study shall focus on imaging magnetic MRs and fabricating suitable designs of such robots thus sufficient reflected polarized light is detected from the target robot for MOI visualization. Additionally, image processing methods should also be improved to enhance MOI system for better sensitivity and image resolution.

Magneto-Acoustic Imaging

Magneto-acoustic tomography (MAI) employs high frequency (MHz range) pulsed magnetic fields to induce vibrations within tissues loaded with magnetic NPs. Particles vibrations produce mechanical waves which are registered through an external transducer and processed to reconstruct

the magnetic material distribution (**Figure 10C**). Differently from MMUS, in which motions induced by continuous low frequency magnetic fields are detected through pulse-echo US sequencing. In MAI the transducer is only used as a receiver. This allows the MAI to have improved imaging bandwidth, limited mainly by the receiving bandwidth of the transducer, leading to better resolution. In addition, as compared to traditional US imaging, acoustic waves in MAI travel shorter paths and experience reduced attenuation in tissues, which leads to improved imaging depth. Because of the pulsed nature of the magnetic excitation signal, MAI allows also to reduce thermal issues related to continuous excitation, featured for instance by MMUS. In addition to basic MAI, magneto-acoustic tomography with magnetic induction has also been proposed (MAI-MI). This latter method combines pulsed fields with static ones to generate acoustic waves through Lorentz force, which can be processed to estimate with high resolution the conductivity distribution of the source. Till now the technique has been employed to either estimate the distribution of magnetic NPs in the FoV, as is the case of simple MAI,[227] or for assessing tissue bioimpedance through MAI-MI.[228] Further research shall consider this technique to push forward tracking of MRs in biological tissues, in order to exploit improved resolution and higher penetration depth compared to other US-based techniques. The main challenges of translating this technology to real-time tracking are related to the improvement of temporal resolution, currently limited by the need of mechanically scanning the transducer at least 180 degrees around the object in order to reconstruct a MAI image. A solution to avoid transducer revolution could be the use of arrays of transducers positioned around the object, although scaling such setup to clinical size is not trivial. Finally, interesting perspectives can be envisioned by the integration of functional materials such as magnetostrictive[229] or magnetoelectric[230] composites, which may enhance US signal or even produce distinct signatures for the detection of MRs.

Improvement of Optical Techniques with Wavefront Shaping

Coherent light that scatters during propagation through tissues forms a speckle pattern. The seemingly random speckle pattern is however deterministic as long as the scattering medium is static.[231–235] The key is the usage of spatial light modulators (SLMs) that are pixelated devices that enable to manipulate the phase of light. If an appropriate mask is displayed on the SLM, it is possible to remove the influence of a scattered field or to pre-shape the incident wavefront to achieve targeted delivery of a light-field distribution through thick scattering tissues (**Figure 10D**).[231,234–237] The huge technological and methodological progress of wavefront shaping techniques allows today for targeted light delivery deep into or through thick biological tissues. It was shown that even entirely scattered light can be controlled and used for imaging or focusing through thick scattering tissues. The only pre-condition is that the mask that is displayed on the SLM is appropriate and fulfills the desired task. It is by far the greatest challenge to obtain information on this phase mask and many solutions like optical phase conjugation,[236,238–240] iterative optimization wavefront shaping,[241,242] and transmission matrix-based[243,244] approaches have been used to achieve this task. It was verified that light can be focused through approx. 100 TMFP, which corresponds to 9.6 cm tissue thickness.[245] However, the above mentioned approaches require physical access through the scattering medium, which makes most of them currently not suitable for real life applications. Most of the work reported in this field showed in a proof-of principle manner that the penetration depth of optical techniques could be dramatically increased using wavefront shaping. The correcting phase mask is just valid, as long the scattering medium is static. After a movement, the calibration has to be repeated. Hence, it is highly desirable to perform the calibration *in-situ*. The required refresh rate depends on the decorrelation time. It was shown in living mouse that the decorrelation time is between 50 ms and 2.5 s depending on the degree of

immobilization and that there is also a strong dependence on the thickness and the type of the tissue, and the setup.[246]

Tracking moving samples through thick scatterers is commonly achieved *via* speckle-correlation techniques, or differences of speckle fields, which yields the movement information, like velocity and moving direction.[247–250] However, with such techniques the exact position and movement in three dimensions is difficult to be extracted quantitatively. A possible way to achieve imaging and tracking in deep-tissue in a minimally invasive manner could be the usage of thin lens-less endoscopes, with diameters <350 µm, that are driven with wavefront shaping techniques.[251,252] Thus, wavefront shaping is a promising tool that will surely lead to further improvement in microscopy techniques, enabling imaging in deep tissues. Employing SLMs allows to do nearly anything with light waves, even to transfer image information through centimeters of tissue. The main task is to find strategies, how to get the required information to determine the appropriate phase mask. When wavefront shaping approaches will be optimized for tracking MRs, this will surely be a step towards clinical applications, as the fundamental limit of light penetration in tissue is not the physics but the technology and methodology in this still infant research topic.

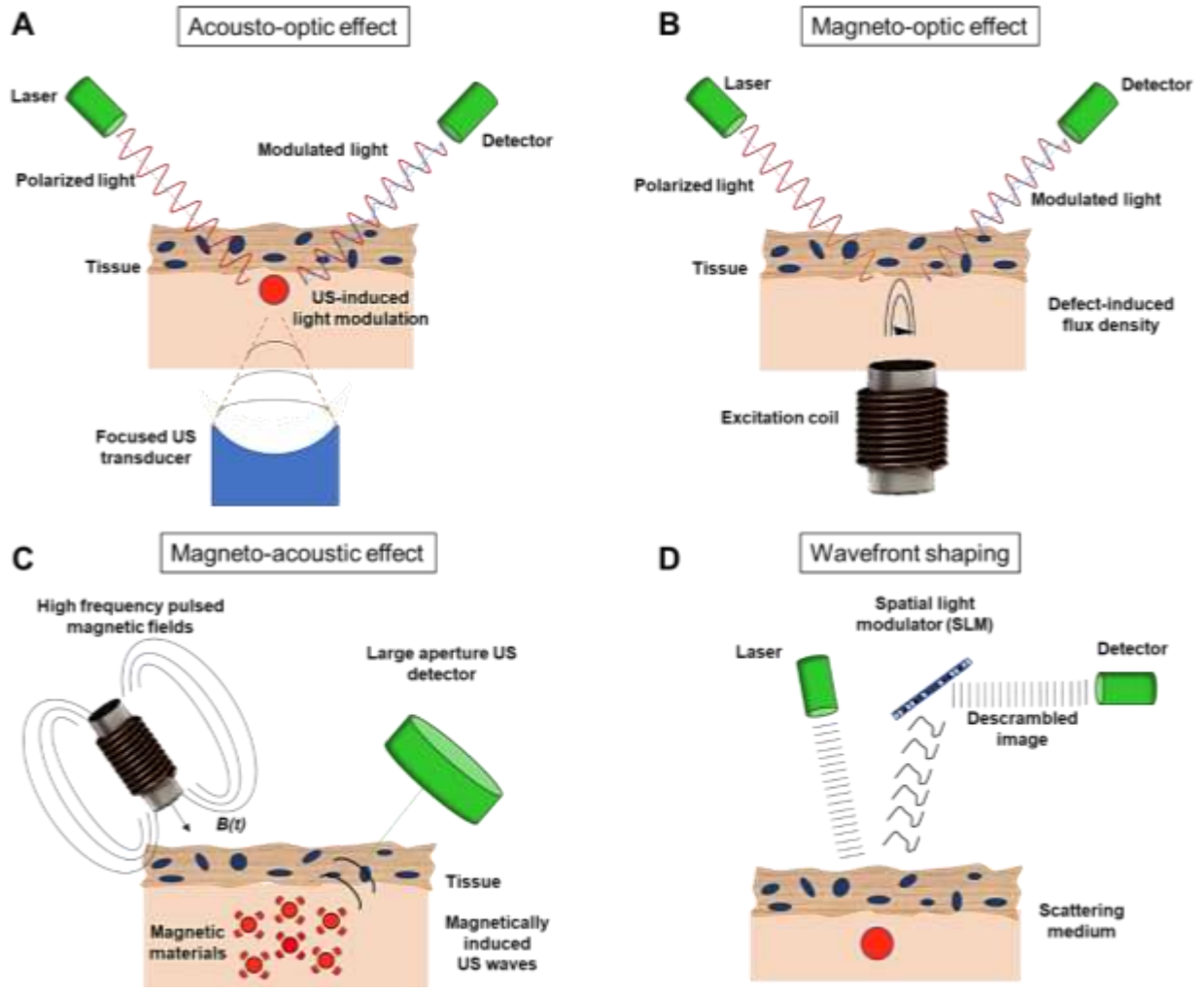

Figure 10. Hybrid techniques for imaging medical MRs and methods for improving optical-based imaging. A) Description of acousto-optic effect: Focused US field modulates polarized light reflected by the sample with information on the medium properties. B) Magneto-optic effect principle: An external excitation coil induces eddy currents in the sample. The presence of defects and cracks in the sample surface generates magnetic flux density which modulates incident polarized light. A CMOS camera detector finally allows to extrapolate information on the sample surface. C) Schematic of the magneto-acoustic effect: High frequency magnetic fields (MHz) induce vibration of magnetic materials which generate US waves. A large aperture US receiver enables to reconstruct magnetic material distribution from detected US pressure. D) Schematic

description of the wavefront shaping technique for imaging through a scattering medium. A sample is illuminated by a laser source and the speckle illuminating the sample returns in phase opposition through the scattering medium. The SLMs manipulate the phase of light by displaying an appropriate mask on the SLMs which remove the influence of a scattered light-field distribution through thick scattering tissues.

AUTHOR INFORMATION

Corresponding Authors

Mariana Medina-Sanchez - *Institute for Integrative Nanosciences, Leibniz IFW Dresden, Helmholtzstrasse 20, 01069 Dresden, Germany*

E-mail: m.medina.sanchez@ifw-dresden.de.

ORCID: 0000-0001-6149-3732

Veronica Iacovacci - *The BioRobotics Institute, Scuola Superiore Sant'Anna, Pisa 50127, and Department of Excellence in Robotics & AI, Scuola Superiore Sant'Anna, 56127 Pisa, Italy*

E-Mail: veronica.iacovacci@santannapisa.it

ORCID: 0000-0002-4052-3581

Authors

Azaam Aziz - *Institute for Integrative Nanosciences, Leibniz IFW Dresden, Helmholtzstrasse 20, 01069 Dresden, Germany; ORCID: 0000-0001-8230-3424*

Stefano Pane - *The BioRobotics Institute, Scuola Superiore Sant'Anna, Pisa 50127, and Department of Excellence in Robotics & AI, Scuola Superiore Sant'Anna, 56127 Pisa, Italy; ORCID: 0000-0002-3740-678X*

Nektarios Koukourakis - *Chair of Measurement and Sensor System Technique, School of Engineering, TU Dresden, Helmholtzstrasse 18, 01069 Dresden, and Center for Biomedical Computational Laser Systems, TU Dresden, Germany; ORCID: 0000-0003-0266-3265*

Jürgen Czarske - *Chair of Measurement and Sensor System Technique, School of Engineering, TU Dresden, Helmholtzstrasse 18, 01069 Dresden, Cluster of Excellence Physics of Life, TU Dresden, and Center for Biomedical Computational Laser Systems, TU Dresden, Germany; ORCID: 0000-0001-7280-0523*

Arianna Menciassi - *The BioRobotics Institute, Scuola Superiore Sant'Anna, Pisa 50127, and Department of Excellence in Robotics & AI, Scuola Superiore Sant'Anna, 56127 Pisa, Italy; ORCID: 0000-0001-6348-1081*

Oliver G. Schmidt - *Institute for Integrative Nanosciences, Leibniz IFW Dresden, Helmholtzstrasse 20, 01069 Dresden, Center for Materials, Architectures and Integration of Nanomembranes (MAIN), TU Chemnitz, Reichenhainer Strasse 10, 09107 Chemnitz, and School of Science, TU Dresden, 01062 Dresden, Germany; ORCID: 0000-0001-9503-8367*

ASSOCIATED CONTENT

The authors declare no competing financial interest.

ACKNOWLEDGEMENTS

The authors thank the priority program of the German Research Foundation SPP 1726 “Microswimmers-From Single Particle Motion to Collective Behavior” for the financial support. O.G.S. acknowledges financial support by the Leibniz Program of the German Research Foundation (SCHM 1298/26-1). This work is part of the projects that have received funding from the European Research Council (ERC) under the European Union’s Horizon 2020 research and innovation program (grant agreement nos. 835268 and 853609). V.I. received funding from the European Union’s Horizon 2020 research and innovation program under the Marie Skłodowska-Curie grant MAMBO, agreement no. 894425. A.M. acknowledges financial support by the European Union’s Horizon 2020 research and innovation program under grant agreement No 825003 – Digital Innovation Hubs in Healthcare Robotics (DIH-HERO).

VOCABULARY

Microrobots: A mobile device several millimetres down to few micrometres in all dimensions appointed to perform specific tasks in a controllable fashion.

Spatial resolution: The minimal object size guaranteeing imaging or alternatively, which is the minimal distance possible between two objects to be discriminated from each other.

Temporal resolution: The minimal time required to complete the data acquisition needed to reconstruct one complete image of the object.

Penetration depth: The measure of how deep the probing signal of an imaging technique can penetrate through tissues. It can be defined as the distance where the primary intensity is reduced to l/e (*i.e.* 37%) of the initial transmitted intensity.

Field of view: The dimensions of the exact anatomic region included in an image.

Contrast agents: A substance to enhance the contrast of structures, bodily fluids or body organs using medical imaging techniques.

Hybrid imaging: It refers to the fusion of two or more imaging techniques to give birth to a more versatile imaging modality.

REFERENCES

(1) Feynman, R. There's Plenty of Room at the Bottom. *Eng. Sci.* **1960**, *23*, 22–36.

(2) Solovev, A. A.; Mei, Y.; Ureña, E. B.; Huang, G.; Schmidt, O. G. Catalytic Microtubular Jet Engines Self-Propelled by Accumulated Gas Bubbles. *Small* **2009**, *5*, 1688–1692.

(3) Sanchez, S.; Soler, L.; Katuri, J. Chemically Powered Micro- and Nanomotors. *Angew. Chem. Int. Ed.* **2015**, *54*, 1414–1444.

(4) Sun, J.; Mathesh, M.; Li, W.; Wilson, D. A. Enzyme-Powered Nanomotors with Controlled Size for Biomedical Applications. *ACS Nano* **2019**, *13*, 10191–10200.

(5) Villa, K.; Krejčová, L.; Novotný, F.; Heger, Z.; Sofer, Z.; Pumera, M. Cooperative Multifunctional Self-Propelled Paramagnetic Microrobots with Chemical Handles for Cell Manipulation and Drug Delivery. *Adv. Funct. Mater.* **2018**, *28*, 1804343.

(6) Zhou, M.; Hou, T.; Li, J.; Yu, S.; Xu, Z.; Yin, M.; Wang, J.; Wang, X. Self-Propelled and Targeted Drug Delivery of Poly(aspartic Acid)/Iron–Zinc Microrocket in the Stomach. *ACS Nano* **2019**, *13*, 1324–1332.

(7) Chen, C.; Soto, F.; Karshalev, E.; Li, J.; Wang, J. Hybrid Nanovehicles: One Machine, Two Engines. *Adv. Funct. Mater.* **2019**, *29*, 1806290.

(8) Llopis-Lorente, A.; García-Fernández, A.; Murillo-Cremaes, N.; Hortelão, A. C.; Patiño, T.; Villalonga, R.; Sancenón, F.; Martínez-Máñez, R.; Sánchez, S. Enzyme-Powered Gated Mesoporous Silica Nanomotors for On-Command Intracellular Payload Delivery. *ACS Nano* **2019**, *13*, 12171–12183.

(9) Srivastava, S. K.; Medina-Sánchez, M.; Schmidt, O. G. Autonomously Propelled Microscavengers for Precious Metal Recovery. *Chem. Commun.* **2017**, *53*, 8140–8143.

(10) Chen, X. Z.; Jang, B.; Ahmed, D.; Hu, C.; De Marco, C.; Hoop, M.; Mushtaq, F.; Nelson, B. J.; Pané, S. Small-Scale Machines Driven by External Power Sources. *Adv. Mater.* **2018**, *30*, 1–22.

(11) Khalil, I. S. M.; Dijkslag, H. C.; Abelmann, L.; Misra, S. MagnetoSperm: A Microrobot That Navigates Using Weak Magnetic Fields. *Appl. Phys. Lett.* **2014**, *104*, 223701

(12) Medina-Sánchez, M.; Schwarz, L.; Meyer, A. K.; Hebenstreit, F.; Schmidt, O. G. Cellular Cargo Delivery: Toward Assisted Fertilization by Sperm-Carrying Micromotors. *Nano Lett.* **2016**, *16*, 555–561.

(13) Srivastava, S. K.; Medina-Sánchez, M.; Koch, B.; Schmidt, O. G. Medibots: Dual-Action Biogenic Microdaggers for Single-Cell Surgery and Drug Release. *Adv. Mater.* **2016**, *28*, 832–837.

(14) Hu, W.; Lum, G. Z.; Mastrangeli, M.; Sitti, M. Small-Scale Soft-Bodied Robot with Multimodal Locomotion. *Nature* **2018**, *554*, 81–85.

(15) Schuerle, S.; Soleimany, A. P.; Yeh, T.; Anand, G. M.; Häberli, M.; Fleming, H. E.; Mirkhani, N.; Qiu, F.; Hauert, S.; Wang, X.; Nelson, B. J.; Bhatia, S. N. Synthetic and Living Micropropellers for Convection-Enhanced Nanoparticle Transport. *Sci. Adv.* **2019**, *5*, 1–11.

(16) Wang, W.; Li, S.; Mair, L.; Ahmed, S.; Huang, T. J.; Mallouk, T. E. Acoustic Propulsion of Nanorod Motors inside Living Cells. *Angew. Chem. Int. Ed.* **2014**, *53*, 3201–3204.

(17) Ahmed, D.; Dillinger, C.; Hong, A.; Nelson, B. J. Artificial Acousto-Magnetic Soft Microswimmers. *Adv. Mater. Technol.* **2017**, *2*, 1–5.

(18) Ahmed, D.; Baasch, T.; Blondel, N.; Läubli, N.; Dual, J.; Nelson, B. J. Neutrophil-Inspired

Propulsion in a Combined Acoustic and Magnetic Field. *Nat. Commun.* **2017**, *8*, 1–8.

(19) Liu, M.; Zentgraf, T.; Liu, Y.; Bartal, G.; Zhang, X. Light-Driven Nanoscale Plasmonic Motors. *Nat. Nanotechnol.* **2010**, *5*, 570-573.

(20) Wu, Z.; Lin, X.; Wu, Y.; Si, T.; Sun, J.; He, Q. Near-Infrared Light-Triggered "On/Off" Motion of Polymer Multilayer Rockets. *ACS Nano* **2014**, *8*, 6097–6105.

(21) Iacovacci, V.; Lucarini, G.; Innocenti, C.; Comisso, N.; Dario, P.; Ricotti, L.; Menciassi, A. Polydimethylsiloxane Films Doped with NdFeB Powder: Magnetic Characterization and Potential Applications in Biomedical Engineering and Microrobotics. *Biomed. Microdevices* **2015**, *17*, 112.

(22) Magdanz, V.; Sanchez, S.; Schmidt, O. G. Development of a Sperm-Flagella Driven Micro-Bio-Robot. *Adv. Mater.* **2013**, *25*, 6581–6588.

(23) Magdanz, V.; Medina-Sánchez, M.; Schwarz, L.; Xu, H.; Elgeti, J.; Schmidt, O. G. Spermatozoa as Functional Components of Robotic Microswimmers. *Adv. Mater.* **2017**, *29*, 1–18.

(24) Stanton, M. M.; Simmchen, J.; Ma, X.; Miguel-López, A.; Sánchez, S. Biohybrid Janus Motors Driven by *Escherichia coli*. *Adv. Mater. Interfaces* **2016**, *3*, 1500505.

(25) Erin, O.; Gilbert, H. B.; Tabak, A. F.; Sitti, M. Elevation and Azimuth Rotational Actuation of an Untethered Millirobot by MRI Gradient Coils. *IEEE Trans. Robot.* **2019**, *35*, 1323–1337.

(26) Park, B. W.; Zhuang, J.; Yasa, O.; Sitti, M. Multifunctional Bacteria-Driven Microswimmers for Targeted Active Drug Delivery. *ACS Nano* **2017**, *11*, 8910–8923.

(27) Schwarz, L.; Medina-Sánchez, M.; Schmidt, O. G. Hybrid BioMicromotors. *Appl. Phys. Rev.* **2017**, *4*, 031301.

(28) Xu, H.; Medina-Sánchez, M.; Magdanz, V.; Schwarz, L.; Hebenstreit, F.; Schmidt, O. G. Sperm-Hybrid Micromotor for Targeted Drug Delivery. *ACS Nano* **2018**, *12*, 327–337.

(29) Nelson, B. J.; Kaliakatsos, I. K.; Abbott, J. J. Microrobots for Minimally Invasive Medicine. *Annu. Rev. Biomed. Eng.* **2010**, *12*, 55–85.

(30) Medina-Sánchez, M.; Xu, H.; Schmidt, O. G. Micro- and Nano-Motors: The New Generation of Drug Carriers. *Ther. Deliv.* **2018**, *9*, 303–316.

(31) Guix, M.; Weiz, S. M.; Schmidt, O. G.; Medina-Sánchez, M. Self-Propelled Micro/Nanoparticle Motors. *Part. Part. Syst. Charact.* **2018**, *35*, 1–31.

(32) Chałupniak, A.; Morales-Narváez, E.; Merkoçi, A. Micro and Nanomotors in Diagnostics. *Adv. Drug Deliv. Rev.* **2015**, *95*, 104–116.

(33) Srivastava, S. K.; Clergeaud, G.; Andresen, T. L.; Boisen, A. Micromotors for Drug Delivery *In Vivo*: The Road Ahead. *Adv. Drug Deliv. Rev.* **2019**, *138*, 41–55.

(34) Ricotti, L.; Cafarelli, A.; Iacovacci, V.; Vannozzi, L.; Menciassi, A. Advanced Micro-Nano-Bio Systems for Future Targeted Therapies. *Curr. Nanosci.* **2015**, *11*, 144–160.

(35) Iacovacci, V.; Lucarini, G.; Ricotti, L.; Dario, P.; Dupont, P. E.; Menciassi, A. Untethered Magnetic Millirobot for Targeted Drug Delivery. *Biomed. Microdevices* **2015**, *17*, 63.

(36) Xi, W.; Solovev, A. A.; Ananth, A. N.; Gracias, D. H.; Sanchez, S.; Schmidt, O. G. Rolled-Up Magnetic Microdrillers: Towards Remotely Controlled Minimally Invasive Surgery. *Nanoscale* **2013**, *5*, 1294–1297.

(37) Vyskočil, J.; C. Mayorga-Martinez, C.; Jablonská, E.; Novotný, F.; Ruml, T.; Pumera, M. Cancer Cells Microsurgery *via* Asymmetric Bent Surface Au/Ag/Ni Microrobotic Scalpels through a Transversal Rotating Magnetic Field. *ACS Nano* **2020**, *14*, 8247-8256.

(38) Guo Sheng Moo, J.; Pumera, M. Self-Propelled Micromotors Monitored by Particle-Electrode Impact Voltammetry. *ACS Sensors* **2016**, *1*, 949–957.

(39) Khezri, B.; Sheng Moo, J. G.; Song, P.; Fisher, A. C.; Pumera, M. Detecting the Complex Motion of Self-Propelled Micromotors in Microchannels by Electrochemistry. *RSC Adv.* **2016**, *6*, 99977–99982.

(40) Esteban-Fernández de Ávila, B.; Lopez-Ramirez, M. A.; Báez, D. F.; Jodra, A.; Singh, V. V; Kaufmann, K.; Wang, J. Aptamer-Modified Graphene-Based Catalytic Micromotors: Off–On Fluorescent Detection of Ricin. *ACS Sensors* **2016**, *1*, 217–221.

(41) Wang, J.; Dong, R.; Wu, H.; Cai, Y.; Ren, B. A Review on Artificial Micro/Nanomotors for Cancer-Targeted Delivery, Diagnosis, and Therapy. *Nano-Micro Lett.* **2020**, *12*. DOI: 10.1007/s40820-019-0350-5

(42) Servant, A.; Qiu, F.; Mazza, M.; Kostarelos, K.; Nelson, B. J. Controlled *In Vivo* Swimming of a Swarm of Bacteria-Like Microrobotic Flagella. *Adv. Mater.* **2015**, *27*, 2981–2988.

(43) Yan, X.; Zhou, Q.; Vincent, M.; Deng, Y.; Yu, J.; Xu, J.; Xu, T.; Tang, T.; Bian, L.; Wang, Y.-X. X. J.; Kostarelos, K.; Zhang, L. Multifunctional Biohybrid Magnetite Microrobots for Imaging-Guided Therapy. *Sci. Robot.* **2017**, *2*, eaaq1155.

(44) Wu, Z.; Li, L.; Yang, Y.; Hu, P.; Li, Y.; Yang, S.-Y.; Wang, L. V.; Gao, W. A Microrobotic System Guided by Photoacoustic Computed Tomography for Targeted

Navigation in Intestines *In Vivo*. *Sci. Robot.* **2019**, *4*, eaax0613.

(45) Gao, W.; Dong, R.; Thamphiwatana, S.; Li, J.; Gao, W.; Zhang, L.; Wang, J. Artificial Micromotors in the Mouse's Stomach: A Step toward *In Vivo* Use of Synthetic Motors. *ACS Nano* **2015**, *9*, 117–123.

(46) Xie, L.; Pang, X.; Yan, X.; Dai, Q.; Lin, H.; Ye, J.; Cheng, Y.; Zhao, Q.; Ma, X.; Zhang, X.; Liu, G.; Chen, X. Photoacoustic Imaging-Trackable Magnetic Microswimmers for Pathogenic Bacterial Infection Treatment. *ACS Nano* **2020**, *14*, 2880–2893.

(47) Medina-Sánchez, M.; Schmidt, O. G. Medical Microbots Need Better Imaging and Control. *Nature* **2017**, *545*, 406–408.

(48) Ullrich, F.; Bergeles, C.; Pokki, J.; Ergeneman, O.; Erni, S.; Chatzipirpiridis, G.; Pané, S.; Framme, C.; Nelson, B. J. Mobility Experiments with Microrobots for Minimally Invasive Intraocular SurgeryMicrorobot Experiments for Intraocular Surgery. *Invest. Ophthalmol. Vis. Sci.* **2013**, *54*, 2853–2863.

(49) Chatzipirpiridis, G.; Ergeneman, O.; Pokki, J.; Ullrich, F.; Fusco, S.; Ortega, J. A.; Sivaraman, K. M.; Nelson, B. J.; Pané, S. Electroforming of Implantable Tubular Magnetic Microrobots for Wireless Ophthalmologic Applications. *Adv. Healthc. Mater.* **2015**, *4*, 209–214.

(50) Felfoul, O.; Mohammadi, M.; Taherkhani, S.; De Lanauze, D.; Zhong Xu, Y.; Loghin, D.; Essa, S.; Jancik, S.; Houle, D.; Lafleur, M.; Radzioch, D.; Martel, S. Magneto-Aerotactic Bacteria Deliver Drug-Containing Nanoliposomes to Tumour Hypoxic Regions. *Nat. Nanotechnol.* **2016**, *11*, 941–947.

(51) Santhi, V.; Acharjya, D. P.; Ezhilarasan, M. *Emerging Technologies in Intelligent*

Applications for Image and Video Processing, 1st ed.; IGI Global: USA, 2016.

(52) Becker, A. T.; Felfoul, O.; Dupont, P. E. Toward Tissue Penetration by MRI-Powered Millirobots Using a Self-Assembled Gauss Gun. In *2015 IEEE International Conference on Robotics and Automation (ICRA)*, IEEE: Seattle, WA, USA, May 26-30, 2015, 1184–1189.

(53) Azizi, A.; Tremblay, C. C.; Gagné, K.; Martel, S. Using the Fringe Field of a Clinical MRI Scanner Enables Robotic Navigation of Tethered Instruments in Deeper Vascular Regions. *Sci. Robot.* **2019**, *4*, eaax7342.

(54) Haacke, E. M.; Li, D.; Kaushikkar, S. Cardiac MR Imaging: Principles and Techniques. *Top. Magn. Reson. Imaging* **1995**, *7* (4), 200—217.

(55) Grover, V. P. B.; Tognarelli, J. M.; Crossey, M. M. E.; Cox, I. J.; Taylor-Robinson, S. D.; McPhail, M. J. W. Magnetic Resonance Imaging: Principles and Techniques: Lessons for Clinicians. *J. Clin. Exp. Hepatol.* **2015**, *5*, 246–255.

(56) Martel, S. Magnetic Nanoparticles in Medical Nanorobotics. *J. Nanoparticle Res.* **2015**, *17*, 75.

(57) Shapiro, E. M.; Skrtic, S.; Sharer, K.; Hill, J. M.; Dunbar, C. E.; Koretsky, A. P. MRI Detection of Single Particles for Cellular Imaging. *Proc. Natl. Acad. Sci. U. S. A.* **2004**, *101*, 10901-10906.

(58) Mathieu, J.-B.; Beaudoin, G.; Martel, S. Method of Propulsion of a Ferromagnetic Core in the Cardiovascular System through Magnetic Gradients Generated by an MRI System. *IEEE Trans. Biomed. Eng.* **2006**, *53*, 292–299.

(59) Martel, S.; Mathieu, J.-B.; Felfoul, O.; Chanu, A.; Aboussouan, E.; Tamaz, S.;

Pouponneau, P.; Yahia, L.; Beaudoin, G.; Soulez, G.; Soulez, G.; Mankiewicz, M. Automatic Navigation of an Untethered Device in the Artery of a Living Animal Using a Conventional Clinical Magnetic Resonance Imaging System. *Appl. Phys. Lett.* **2007**, *90*, 114105.

(60) Mathieu, J.-B.; Martel, S. Magnetic Steering of Iron Oxide Microparticles Using Propulsion Gradient Coils in MRI. In *2006 Annual International Conference of the IEEE Engineering in Medicine and Biology*, IEEE: New York, USA, 30 Aug.-3 Sept., 2006, 472–475.

(61) Martel, S.; Mohammadi, M.; Felfoul, O.; Zhao Lu; Pouponneau, P. Flagellated Magnetotactic Bacteria as Controlled MRI-Trackable Propulsion and Steering Systems for Medical Nanorobots Operating in the Human Microvasculature. *Int. J. Rob. Res.* **2009**, *28*, 571–582.

(62) Kósa, G.; Jakab, P.; Székely, G.; Hata, N. MRI Driven Magnetic Microswimmers. *Biomed. Microdevices* **2012**, *14*, 165–178.

(63) Belharet, K.; Folio, D.; Ferreira, A. MRI-Based Microrobotic System for the Propulsion and Navigation of Ferromagnetic Microcapsules. *Minim. Invasive Ther. Allied Technol.* **2010**, *19*, 157–169.

(64) Felfoul, O.; Mohammadi, M.; Taherkhani, S.; De Lanauze, D.; Zhong Xu, Y.; Loghin, D.; Essa, S.; Jancik, S.; Houle, D.; Lafleur, M.; Gaboury, L.; Tabrizian, M.; Kaou, N.; Atkin, M.; Vuong, T.; Batist, G.; Beauchemin, N.; Radzioch, D.; Martel, S. Magneto-Aerotactic Bacteria Deliver Drug-Containing Nanoliposomes to Tumour Hypoxic Regions. *Nat. Nanotechnol.* **2016**, *11*, 941–947.

(65) Martel, S.; Felfoul, O.; Mathieu, J.-B.; Chanu, A.; Tamaz, S.; Mohammadi, M.; Mankiewicz, M.; Tabatabaei, N. MRI-Based Medical Nanorobotic Platform for the Control of Magnetic Nanoparticles and Flagellated Bacteria for Target Interventions in Human Capillaries. *Int. J. Rob. Res.* **2009**, *28*, 1169–1182.

(66) Tabatabaei, S. N.; Lapointe, J.; Martel, S. Shrinkable Hydrogel-Based Magnetic Microrobots for Interventions in the Vascular Network. *Adv. Robot.* **2011**, *25*, 1049–1067.

(67) Dahmen, C.; Belharet, K.; Folio, D.; Ferreira, A.; Fatikow, S. MRI-Based Dynamic Tracking of an Untethered Ferromagnetic Microcapsule Navigating in Liquid. *Int. J. Optomechatronics* **2016**, *10*, 73–96.

(68) Pouponneau, P.; Leroux, J.-C.; Soulez, G.; Gaboury, L.; Martel, S. Co-Encapsulation of Magnetic Nanoparticles and Doxorubicin into Biodegradable Microcarriers for Deep Tissue Targeting by Vascular MRI Navigation. *Biomaterials* **2011**, *32*, 3481–3486.

(69) Martel, S. Magnetic Navigation Control of Microagents in the Vascular Network: Challenges and Strategies for Endovascular Magnetic Navigation Control of Microscale Drug Delivery Carriers. *IEEE Control Syst. Mag.* **2013**, *33*, 119–134.

(70) Gleich, B.; Weizenecker, J. Tomographic Imaging Using the Nonlinear Response of Magnetic Particles. *Nature* **2005**, *435*, 1214–1217.

(71) Borgert, J.; Schmidt, J. D.; Schmale, I.; Rahmer, J.; Bontus, C.; Gleich, B.; David, B.; Eckart, R.; Woywode, O.; Weizenecker, J. Fundamentals and Applications of Magnetic Particle Imaging. *J. Cardiovasc. Comput. Tomogr.* **2012**, *6*, 149–153.

(72) Nothnagel, N.; Rahmer, J.; Gleich, B.; Halkola, A.; Buzug, T. M.; Borgert, J. Steering of Magnetic Devices with a Magnetic Particle Imaging System. *IEEE Trans. Biomed. Eng.*

2016, *63*, 2286–2293.

(73) Rahmer, J.; Stehning, C.; Gleich, B. Remote Magnetic Actuation Using a Clinical Scale System. *PLoS One* **2018**, *13*, 1–19.

(74) Gräser, M.; Thieben, F.; Szwargulski, P.; Werner, F.; Gdaniec, N.; Boberg, M.; Griese, F.; Möddel, M.; Ludewig, P.; van de Ven, D.; Weber, O. M.; Woywode, O.; Gleich, B.; Knopp, T. Human-Sized Magnetic Particle Imaging for Brain Applications. *Nat. Commun.* **2019**, *10*, 1936.

(75) Bakenecker, A. C.; von Gladiss, A.; Friedrich, T.; Heinen, U.; Lehr, H.; Lüdtke-Buzug, K.; Buzug, T. M. Actuation and Visualization of a Magnetically Coated Swimmer with Magnetic Particle Imaging. *J. Magn. Magn. Mater.* **2019**, *473*, 495–500.

(76) Griese, F.; Knopp, T.; Gruettner, C.; Thieben, F.; Müller, K.; Loges, S.; Ludewig, P.; Gdaniec, N. Simultaneous Magnetic Particle Imaging and Navigation of Large Superparamagnetic Nanoparticles in Bifurcation Flow Experiments. *J. Magn. Magn. Mater.* **2020**, *498*, 166206.

(77) Kremkau, F. W. *Diagnostic Ultrasound: Principles and Instruments*; 4th ed. WB Saunders Philadelphia, 1998.

(78) Calliada, F.; Campani, R.; Bottinelli, O.; Bozzini, A.; Sommaruga, M. G. Ultrasound Contrast Agents: Basic Principles. *Eur. J. Radiol.* **1998**, *27*, 157-160.

(79) Nasoni, R. L. Temperature Corrected Speed of Sound for Use in Soft Tissue Imaging. *Med. Phys.* **1981**, *8*, 513–515.

(80) Liebgott, H.; Rodriguez-Molares, A.; Cervenansky, F.; Jensen, J. A.; Bernard, O. Plane-Wave Imaging Challenge in Medical Ultrasound. In *IEEE International Ultrasonics*

Symposium (IUS), IEEE: Tours, France, Sept. 18-21, 2016, 1-4.

(81) Azhari, H. *Basics of Biomedical Ultrasound for Engineers*, Third Edition, Wiley Online Books Series, John Wiley & Sons, Inc.: Hoboken, New Jersey, 2010, Vol. 1, 1-371.

(82) Hunt, J. W.; Arditi, M.; Foster, F. S. Ultrasound Transducers for Pulse-Echo Medical Imaging. *IEEE Trans. Biomed. Eng.* **1983**, *30*, 453–481.

(83) Khalil, I. S. M. M.; Ferreira, P.; Eleutério, R.; De Korte, C. L.; Misra, S.; Korte, C. L. de; Misra, S. Magnetic-Based Closed-Loop Control of Paramagnetic Microparticles Using Ultrasound Feedback. In *2014 International Conference on Robotics and Automation (ICRA)*, IEEE: Hong Kong, China, 31 May-7 June, 2014, 3807–3812.

(84) Sánchez, A.; Magdanz, V.; Schmidt, O. G.; Misra, S. Magnetic Control of Self-Propelled Microjets under Ultrasound Image Guidance. In *RAS EMBS International Conference on Biomedical Robotics and Biomechatronics*, IEEE: Sao Paulo, Brazil, Aug. 12-15, 2014, 169–174.

(85) Scheggi, S.; Yoon, C. K.; Ghosh, A.; Gracias, D. H.; Misra, S. A GPU-Accelerated Model-Based Tracker for Untethered Submillimeter Grippers. *Rob. Auton. Syst.* **2018**, *103*, 111–121.

(86) Ongaro, F.; Niehoff, D.; Mohanty, S.; Misra, S. A Contactless and Biocompatible Approach for 3D Active Microrobotic Targeted Drug Delivery. *Micromachines* **2019**, *10*, 504.

(87) Dandan Li, Moonkwang Jeong, Eran Oren, Tingting Yu, T. Q. A Helical Microrobot with an Optimized Propeller-Shape for Propulsion in Viscoelastic Biological Media. *MDPI, Robot.* **2019**, *8*, 87.

(88) Bi, C.; Niedert, E. E.; Adam, G.; Lambert, E.; Solorio, L.; Goergen, C. J.; Cappelleri, D. J. Tumbling Magnetic Microrobots for Biomedical Applications. In *2019 International Conference on Manipulation, Automation, and Robotics at Small Scales (MARSS)*, IEEE: Helsinki, Finland, July 1-5, 2019, 1–6.

(89) Xie, H.; Sun, M.; Fan, X.; Lin, Z.; Chen, W.; Wang, L.; Dong, L.; He, Q. Reconfigurable Magnetic Microrobot Swarm: Multimode Transformation, Locomotion, and Manipulation. *Microrobots* **2019**, 1–15.

(90) Yigit, B.; Alapan, Y.; Sitti, M. Programmable Collective Behavior in Dynamically Self-Assembled Mobile Microrobotic Swarms. *Adv. Sci.* **2019**, *6*, *1801837*.

(91) Yu, J.; Wang, B.; Du, X.; Wang, Q.; Zhang, L. Ultra-Extensible Ribbon-like Magnetic Microswarm. *Nat. Commun.* **2018**, *9*, 1–9.

(92) Wang, Q.; Yang, L.; Yu, J.; Wai, P.; Chiu, Y. Magnetic Navigation of a Rotating Colloidal Swarm Using Ultrasound Images. 2018, 1809.06501. axXiv. https://arxiv.org/abs/1809.06501

(93) Yu, J.; Wang, Q.; Li, M.; Liu, C.; Wang, L.; Xu, T.; Zhang, L. Characterizing Nanoparticle Swarms with Tuneable Concentrations for Enhanced Imaging Contrast. *IEEE Robot. Autom. Lett.* **2019**, *4*, 2942–2949.

(94) Yu, J.; Jin, D.; Chan, K. F.; Wang, Q.; Yuan, K.; Zhang, L. Active Generation and Magnetic Actuation of Microrobotic Swarms in Bio-Fluids. *Nat. Commun.* **2019**, *10*, 5631.

(95) Qianqian Wang, Jiangfan Yu, K. Y. Disassembly and Spreading of Magnetic Nanoparticle Clusters on Uneven Surfaces. *Appl. Mater. Today* **2019**, *1*, 1–6.

(96) Singh, A. V.; Dad Ansari, M. H.; Dayan, C. B.; Giltinan, J.; Wang, S.; Yu, Y.; Kishore,

V.; Laux, P.; Luch, A.; Sitti, M. Multifunctional Magnetic Hairbot for Untethered Osteogenesis, Ultrasound Contrast Imaging and Drug Delivery. *Biomaterials* **2019**, *219*, 119394.

(97) Liberman, A.; Wang, J.; Lu, N.; Viveros, R. D.; Allen, C. A.; Mattrey, R. F.; Blair, S. L.; Trogler, W. C.; Kim, M. J.; Kummel, A. C. Mechanically Tunable Hollow Silica Ultrathin Nanoshells for Ultrasound Contrast Agents. *Adv. Funct. Mater.* **2015**, *25*, 4049–4057.

(98) Nagy, Z.; Flückiger, M.; Ergeneman, O.; Pané, S.; Probst, M.; Nelson, B. J. A Wireless Acoustic Emitter for Passive Localization in Liquids. In *2009 International Conference on Robotics and Automation*, IEEE: Kobe, Japan, May 12-17, 2009, 2593–2598.

(99) Flückiger, M.; Nelson, B. J. Ultrasound Emitter Localization in Heterogeneous Media. *Annu. Int. Conf. IEEE Eng. Med. Biol. - Proc.* **2007**, 2867–2870.

(100) Steinberg, I.; Ben-David, M.; Gannot, I. A New Method for Tumor Detection Using Induced Acoustic Waves from Tagged Magnetic Nanoparticles. *Nanomedicine* **2011**, *8*, 569–579.

(101) Lin, F.; Shelton, S. E.; Espíndola, D.; Rojas, J. D.; Pinton, G.; Dayton, P. A. 3-D Ultrasound Localization Microscopy for Identifying Microvascular Morphology Features of Tumor Angiogenesis at a Resolution beyond the Diffraction Limit of Conventional Ultrasound. *Theranostics* **2017**, *7*, 196–204.

(102) Yu, J.; Lavery, L.; Kim, K. Super-Resolution Ultrasound Imaging Method for Microvasculature *In Vivo* with a High Temporal Accuracy. *Sci. Rep.* **2018**, 8, 13918.

(103) Liu, Y.; Yang, Y.; Shu, Y.; Zhou, T.; Luo, J.; Liu, X. Super-Resolution Ultrasound Imaging by Sparse Bayesian Learning Method. *IEEE Access* **2019**, *7*, 47197–47205.

(104) Guo, W.; Tong, Y.; Huang, Y.; Wang, Y.; Yu, J. A High-Efficiency Super-Resolution Reconstruction Method for Ultrasound Microvascular Imaging. *Appl. Sci.* **2018**, *8*, 1143.

(105) van Sloun, R. J. G.; Solomon, O.; Bruce, M.; Khaing, Z. Z.; Wijkstra, H.; Eldar, Y. C.; Mischi, M. Super-Resolution Ultrasound Localization Microscopy through Deep Learning. 2018, 1804.07661, arXiv. https://arxiv.org/abs/1804.07661

(106) Adebar, T. K.; Fletcher, A. E.; Okamura, A. M. 3-D Ultrasound-Guided Robotic Needle Steering in Biological Tissue. *IEEE Trans. Biomed. Eng.* **2014**, *61*, 2899–2910.

(107) Fronheiser, M. P.; Idriss, S. F.; Wolf, P. D.; Smith, S. W. Vibrating Interventional Device Detection Using Real-Time 3-D Color Doppler. *IEEE Trans. Ultrason. Ferroelectr. Freq. Control* **2008**, *55*, 1355–1362.

(108) Gigan, S. Optical Microscopy Aims Deep. *Nat. Photonics* **2017**, *11*, 14–16.

(109) Ntziachristos, V. Going Deeper than Microscopy: The Optical Imaging Frontier in Biology. *Nat. Methods* **2010**, *7*, 603–614.

(110) Smith, A. M.; Mancini, M. C.; Nie, S. Bioimaging: Second Window for *In Vivo* Imaging. *Nat. Nanotechnol.* **2009**, *4*, 710–711.

(111) Loebich, O. The Optical Properties of Gold. *Gold Bull.* **1972**, *5*, 2–10.

(112) White, J. G.; Amos, W. B. Confocal Microscopy Comes of Age. *Nature* **1987**, *328*, 183–184.

(113) Koukourakis, N.; Finkeldey, M.; Stürmer, M.; Leithold, C.; Gerhardt, N. C.; Hofmann, M. R.; Wallrabe, U.; Czarske, J. W.; Fischer, A. Axial Scanning in Confocal Microscopy Employing Adaptive Lenses (CAL). *Opt. Express* **2014**, *22*, 6025.

(114) Huang, D.; Swanson, E. A.; Lin, C. P.; Schuman, J. S.; Stinson, W. G.; Chang, W.; Hee, M. R.; Flotire, T.; Gregory, K.; Puliafito, C. A.; Fujimoto, J. G. Optical Coherence Tomography. *Science.* **1991**, *254*, 1178–1181.

(115) Chong, S. P.; Merkle, C. W.; Cooke, D. F.; Zhang, T.; Radhakrishnan, H.; Krubitzer, L.; Srinivasan, V. J. Noninvasive, *In Vivo* Imaging of Subcortical Mouse Brain Regions with 17 Mm Optical Coherence Tomography. *Opt. Lett.* **2015**, *40*, 4911.

(116) Li, B.; Wang, H.; Fu, B.; Wang, R.; Sakadzic, S.; Boas, D. A. Impact of Temporal Resolution on Estimating Capillary RBC-Flux with Optical Coherence Tomography. *J. Biomed. Opt*. **2017**, *22*, 16014.

(117) Yaqoob, Z.; Wu, J.; Yang, C. Spectral Domain Optical Coherence Tomography: A Better OCT Imaging Strategy. *Biotechniques* **2005**, *39*, 6-13.

(118) Li, D.; Dong, D.; Lam, W.; Xing, L.; Wei, T.; Sun, D. Automated *In Vivo* Navigation of Magnetic-Driven Microrobots Using OCT Imaging Feedback. *IEEE Trans. Biomed. Eng.* **2019**, *67*, 2349-2358.

(119) Zhang, J.; Liu, J.; Wang, L. M.; Li, Z. Y.; Yuan, Z. Retroreflective-Type Janus Microspheres as a Novel Contrast Agent for Enhanced Optical Coherence Tomography. *J. Biophotonics* **2017**, *10*, 878–886.

(120) Han, Y. D.; Kim, H. S.; Park, Y. M.; Chun, H. J.; Kim, J. H.; Yoon, H. C. Retroreflective Janus Microparticle as a Nonspectroscopic Optical Immunosensing Probe. *ACS Appl. Mater. Interfaces* **2016**, *8*, 10767-10774.

(121) Bergeles, C.; Kratochvil, B. E.; Nelson, B. J. Visually Servoing Magnetic Intraocular Microdevices. *IEEE Trans. Robot.* **2012**, *28*, 798–809.

(122) Aziz, A.; Medina-Sánchez, M.; Koukourakis, N.; Wang, J.; Kuschmierz, R.; Radner, H.; Czarske, J. W.; Schmidt, O. G. Real-Time IR Tracking of Single Reflective Micromotors through Scattering Tissues. *Adv. Funct. Mater.* **2019**, *29*, 1905272.

(123) Jabłoński, A. Efficiency of Anti-Stokes Fluorescence in Dyes. *Nature* **1993**, *131*, 839–840.

(124) Helmchen, F.; Denk, W. Deep Tissue Two-Photon Microscopy. *Nat. Methods* **2005**, *2*, 932–940.

(125) ICNIRP. Icnirp Guidelines on Limits of Exposure to Incoherent Visible and Infrared Radiation. *Health Phys.* **2013**, *71*, 804–819.

(126) Steager, E. B.; Sakar, M. S.; Magee, C.; Kennedy, M.; Cowley, A.; Kumar, V. Automated Biomanipulation of Single Cells Using Magnetic Microrobots. *Int. J. Rob. Res.* **2013**, *32*, 346–359.

(127) Nat, A. Y.; Ueno, T.; Nagano, T. Fluorescent Probes for Sensing and Imaging. *Nat. Publ. Gr.* **2011**, *8*, 642–645.

(128) Schnermann, M. J. Organic Dyes for Deep Bioimaging. *Nature* **2017**, *551*, 176.

(129) Walling, M. A.; Novak, J. A.; Shepard, J. R. E. Quantum Dots for Live Cell and *In Vivo* Imaging. *Int. J. Mol. Sci*. **2009**, *10*, 441–491.

(130) Alivisatos, A. P. Semiconductor Clusters, Nanocrystals, and Quantum Dots. *Science*, **1996**, *271*, 933–937.

(131) Fernandez-Bravo, A.; Yao, K.; Barnard, E. S.; Borys, N. J.; Levy, E. S.; Tian, B.; Tajon, C. A.; Moretti, L.; Altoe, M. V.; Aloni, S.; Beketayev, K.; Scotognella, F.; Cohen, B. E.; Chan, E. M.; Schuck, P. J. Continuous-Wave Upconverting Nanoparticle Microlasers. *Nat.*

Nanotechnol. **2018**, *13*, 572–577.

(132) Pai, J.-H.; Wang, Y.; To'A Salazar, G.; E. Sims, C.; Bachman, M.; P. Li, G.; L. Allbritton, N. Photoresist with Low Fluorescence for Bioanalytical Applications. *Anal. Chem.* **2007**, *79*, 8774–8780.

(133) Jurado-Sanchez, B.; Pacheco, M.; Rojo, J.; Escarpa, A. Magnetocatalytic Graphene Quantum Dots Janus Micromotors for Bacterial Endotoxin Detection. *Angew. Chem. Int. Ed. Engl.* **2017**, *56*, 6957–6961.

(134) Lusic, H., & Grinstaff, M. W., X-ray-Computed Tomography Contrast Agents. *Chem. Rev.* **2013**, *113*, 1641-1666.

(135) Nikolaou, K.; Flohr, T.; Knez, A.; Rist, C.; Wintersperger, B.; Johnson, T.; Reiser, M. F.; Becker, C. R. Advances in Cardiac CT Imaging: 64-Slice Scanner. *Int. J. Cardiovasc. Imaging* **2004**, *20*, 535–540.

(136) Vedantham, S.; Karellas, A.; Suryanarayanan, S. Solid-State Fluoroscopic Imager for High-Resolution Angiography: Parallel-Cascaded Linear Systems Analysis. *Med. Phys.* **2004**, *31*, 1258–1268.

(137) Reed, K. B.; Majewicz, A.; Kallem, V.; Alterovitz, R.; Goldberg, K.; Cowan, N. J.; Okamura, A. M. Robot-Assisted Needle Steering. *IEEE Robot. Autom. Mag.* **2011**, *18*, 35–46.

(138) Glozman, D.; Shoham, M. Image-Guided Robotic Flexible Needle Steering. *IEEE Trans. Robot.* **2007**, *23*, 459–467.

(139) Hong, A.; Petruska, A. J.; Nelson, B. J. Tracking a Magnetically Guided Catheter with a Single Rotating C-Arm. In *2015 IEEE International Conference on Robotics and*

Automation (ICRA), IEEE: Seattle, WA, USA, May 26-30, 2015, 618–623.

(140) Nguyen, P. B.; Kang, B.; Bappy, D. M.; Choi, E.; Park, S.; Ko, S. Y.; Park, J.-O.; Kim, C.-S. Real-Time Microrobot Posture Recognition *via* Biplane X-Ray Imaging System for External Electromagnetic Actuation. *Int. J. Comput. Assist. Radiol. Surg.* **2018**, *13*, 1843–1852.

(141) Jeong, S.; Choi, H.; Go, G.; Lee, C.; Lim, K. S.; Sim, D. S.; Jeong, M. H.; Ko, S. Y.; Park, J.-O.; Park, S. Penetration of an Artificial Arterial Thromboembolism in a Live Animal Using an Intravascular Therapeutic Microrobot System. *Med. Eng. Phys.* **2016**, *38*, 403–410.

(142) Xu, Z.; Chen, M.; Lee, H.; Feng, S.-P.; Park, J. Y.; Lee, S.; Kim, J. T. X-Ray Powered Micromotors. *ACS Appl. Mater. Interfaces* **2019**, *11*, 15727-15732.

(143) Wållberg, H.; Ståhl, S. Design and Evaluation of Radiolabeled Tracers for Tumor Imaging. *Biotechnol. Appl. Biochem.* **2013**, *60*, 365–383.

(144) Llop, J.; Gómez-Vallejo, V.; Gibson, N. Quantitative Determination of the Biodistribution of Nanoparticles: Could Radiolabeling Be the Answer? *Nanomedicine* **2013**, *8*, 1035–1038.

(145) Müller, C.; Schibli, R. Single Photon Emission Computed Tomography Tracer. In *Molecular Imaging in Oncology*; Schober, O., Riemann, B., Eds.; Springer Berlin Heidelberg: Berlin, Heidelberg, 2013; pp 65–105.

(146) Rahmim, A.; Zaidi, H. PET *versus* SPECT: Strengths, Limitations and Challenges. *Nucl. Med. Commun.* **2008**, *29*, 193-207.

(147) Vilela, D.; Cossío, U.; Parmar, J.; Martínez-Villacorta, A. M.; Gómez-Vallejo, V.; Llop, J.;

Sánchez, S.; Martínez, A. M.; Llop, J.; Sanchez, S. Medical Imaging for the Tracking of Micromotors. *ACS Nano* **2018**, *12*, 1220–1227.

(148) Iacovacci, V.; Blanc, A.; Huang, H.; Ricotti, L.; Schibli, R.; Menciassi, A.; Behe, M.; Pané, S.; Nelson, B. J. High-Resolution SPECT Imaging of Stimuli-Responsive Soft Microrobots. *Small* **2019**, *15*, 1900709.

(149) Iacovacci, V.; Blanc, A.; Huang, H.; Ricotti, L.; Schibli, R.; Menciassi, A.; Behe, M.; Pané, S.; Nelson, B. J. High-Resolution SPECT Imaging of Stimuli-Responsive Soft Microrobots. *Small* **2019**, *15*, 1900709.

(150) Taruttis, A.; Ntziachristos, V. Advances in Real-Time Multispectral Optoacoustic Imaging and Its Applications. *Nat. Photonics* **2015**, *9*, 219–227.

(151) Omar, M.; Aguirre, J.; Ntziachristos, V. Optoacoustic Mesoscopy for Biomedicine. *Nat. Biomed. Eng.* **2019**, *3*, 354–370.

(152) Zhao, T.; Desjardins, A. E.; Ourselin, S.; Vercauteren, T.; Xia, W. Minimally Invasive Photoacoustic Imaging: Current Status and Future Perspectives. *Photoacoustics* **2019**, *16*, 100146.

(153) Beard, P. Biomedical Photoacoustic Imaging. *Interface Focus* **2011**, *1*, 602–631.

(154) Alexander Graham Bell. The Production of Sound by Radiant Energy. *Science,* **1881**, *2*, 242-253.

(155) Zhou, Y.; Yao, J.; Wang, L. V. Tutorial on Photoacoustic Tomography. *J. Biomed. Opt.* **2016**, *21*, 61007.

(156) Upputuri, P. K.; Pramanik, M. Recent Advances toward Preclinical and Clinical

Translation of Photoacoustic Tomography: A Review. *J. Biomed. Opt.* **2017**, *22*, 41006.

(157) Attia, A. B. E.; Chuah, S. Y.; Razansky, D.; Ho, C. J. H.; Malempati, P.; Dinish, U. S.; Bi, R.; Fu, C. Y.; Ford, S. J.; Lee, J. S.-S.; Tan, M. W. P.; Olivo, M.; Thng, S. T. G. Noninvasive Real-Time Characterization of Non-Melanoma Skin Cancers with Handheld Optoacoustic Probes. *Photoacoustics* **2017**, *7*, 20–26.

(158) Zhou, Y.; Tripathi, S. V.; Rosman, I.; Ma, J.; Hai, P.; Linette, G. P.; Council, M. L.; Fields, R. C.; Wang, L. V.; Cornelius, L. A. Noninvasive Determination of Melanoma Depth Using a Handheld Photoacoustic Probe. *J. Invest. Dermatol.* **2017**, *137*, 1370–1372.

(159) Wu, D.; Huang, L.; Jiang, M. S.; Jiang, H. Contrast Agents for Photoacoustic and Thermoacoustic Imaging: A Review. *Int. J. Mol. Sci.* **2014**, *15*, 23616–23639.

(160) Oraevsky, A. A. "Contrast Agents for Optoacoustic Imaging: Design and Biomedical Applications." *Photoacoustics* **2015**, *3*, 1–2.

(161) Xu, M.; Wang, L. V. Universal Back-Projection Algorithm for Photoacoustic Computed Tomography. *Phys. Rev. E - Stat. Nonlinear, Soft Matter Phys.* **2005**, *71*, 16706.

(162) Lutzweiler, C.; Deán-Ben, X. L.; Razansky, D. Expediting Model-Based Optoacoustic Reconstructions with Tomographic Symmetries. *Med. Phys.* **2014**, *41*, 13302.

(163) Razansky, D.; Distel, M.; Vinegoni, C.; Ma, R.; Perrimon, N.; Köster, R. W.; Ntziachristos, V. Multispectral Opto-Acoustic Tomography of Deep-Seated Fluorescent Proteins *In Vivo*. *Nat. Photonics* **2009**. *3*, 412-417.

(164) Ntziachristos, V.; Razansky, D. Molecular Imaging by Means of Multispectral Optoacoustic Tomography (MSOT). *Chem. Rev.* **2010**, *110*, 2783–2794.

(165) Merčep, E.; Deán-Ben, X. L.; Razansky, D. Imaging of Blood Flow and Oxygen State with a Multi-Segment Optoacoustic Ultrasound Array. *Photoacoustics* **2018**, *10*, 48–53.

(166) Prakash, J.; Raju, A. S.; Shaw, C. B.; Pramanik, M.; Yalavarthy, P. K. Basis Pursuit Deconvolution for Improving Model-Based Reconstructed Images in Photoacoustic Tomography. *Biomed. Opt. Express* **2014**, *5*, 1363–1377.

(167) Kruger, R. A.; Reinecke, D. R.; Kruger, G. A. Thermoacoustic Computed Tomography-Technical Considerations. *Med. Phys.* **1999**, *26*, 1832–1837.

(168) Huang, H.; Bustamante, G.; Peterson, R.; Ye, J. Y. An Adaptive Filtered Back-Projection for Photoacoustic Image Reconstruction. *Med. Phys.* **2015**, *42*, 2169–2178.

(169) Haltmeier, M.; Neumann, L.; Rabanser, S. Single-Stage Reconstruction Algorithm for Quantitative Photoacoustic Tomography. *Inverse Probl.* **2015**, *31*, 065005.

(170) Dean-Ben, X. L.; Fehm, T. F.; Gostic, M.; Razansky, D.; Deán-Ben, X. L.; Fehm, T. F.; Gostic, M.; Razansky, D. Volumetric Hand-Held Optoacoustic Angiography as a Tool for Real-Time Screening of Dense Breast. *J. Biophotonics* **2016**, *9*, 253–259.

(171) Aziz, A.; Medina-Sánchez, M.; Claussen, J.; Schmidt, O. G. Real-Time Optoacoustic Tracking of Single Moving Micro-Objects in Deep Phantom and *Ex Vivo* Tissues. *Nano Lett.* **2019**, *19*, 6612–6620.

(172) Aziz, A.; Medina-Sánchez, M.; Claussen, J.; Schmidt, O. G. Real-Time Optoacoustic Tracking of Single Moving Micro-Objects in Deep Tissue-Mimicking Phantoms. 2019, 1907.09264, arXiv. https://arxiv.org/abs/1907.09264.

(173) Aziz, A.; Medina-Sanchez, M.; Claussen, J.; Schmidt, O. G. Optoacoustic Detection of 3D Microstructures in Deep Tissue-Mimicking Phantoms, In *2019 International Conference*

on Manipulation, Automation, and Robotics at Small Scales (MARSS), IEEE: Helsinki, Finland, July 1-5, 2019, 1–6.

(174) Li, J.; Thamphiwatana, S.; Liu, W.; Esteban-Fernandez De Avila, B.; Angsantikul, P.; Sandraz, E.; Wang, J. J.; Xu, T.; Soto, F.; Ramez, V. Wang, X.; Gao, W.; Zhang, L.; Wang, J. Enteric Micromotor Can Selectively Position and Spontaneously Propel in the Gastrointestinal Tract. *ACS Nano* **2016**, *10*, 9536–9542.

(175) Laufer, J.; Johnson, P.; Zhang, E.; Treeby, B.; Cox, B.; Pedley, B.; Beard, P. *In Vivo* Preclinical Photoacoustic Imaging of Tumor Vasculature Development and Therapy. *J. Biomed. Opt.* **2012**, *17*, 056016.

(176) Park, S.; Jang, J.; Kim, J.; Kim, Y. S.; Kim, C. Real-Time Triple-Modal Photoacoustic, Ultrasound, and Magnetic Resonance Fusion Imaging of Humans. *IEEE Trans. Med. Imaging* **2017**, *36*, 1912–1921.

(177) Lee, D.; Lee, C.; Kim, S.; Zhou, Q.; Kim, J.; Kim, C. *In Vivo* Near Infrared Virtual Intraoperative Surgical Photoacoustic Optical Coherence Tomography. *Sci. Rep.* **2016**, *6*, 35176.

(178) Yan, Y.; Jing, W.; Mehrmohammadi, M. Submillimeter Magnetic Microrobot Tracking Using an Integrated Ultrasound and Photoacoustic Imaging System, In *2019 IEEE International Ultrasonics Symposium (IUS)*, IEEE: Glagow, United Kingdom, Oct. 6-9, 2019, 1057–1060.

(179) Aziz, A.; Holthof, J.; Meyer, S.; Schmidt, O. G.; Medina-Sánchez, M. *In Vivo* Imaging of Swimming Micromotors Using Hybrid High-Frequency Ultrasound and Photoacoustic Imaging. 2020, bioRxiv. https://doi.org/10.1101/2020.06.15.148791.

(180) Oh, J.; Feldman, M. D.; Kim, J.; Condit, C.; Emelianov, S.; Milner, T. E. Detection of Magnetic Nanoparticles in Tissue Using Magneto-Motive Ultrasound. *Nanotechnology* **2006**, *17*, 4183–4190.

(181) Mehrmohammadi, M.; Shin, T.-H.; Qu, M.; Kruizinga, P.; Truby, R. L.; Lee, J.-H.; Cheon, J.; Emelianov, S. Y. *In Vivo* Pulsed Magneto-Motive Ultrasound Imaging Using High-Performance Magnetoactive Contrast Nanoagents. *Nanoscale* **2013**, *5*, 11179–11186.

(182) Kranemann, T. C.; Ersepke, T.; Schmitz, G. Magnetomotive Ultrasound Imaging Using the Nonlinear Magnetization of Nanoparticles. In *IEEE International Ultrasonics Symposium, (IUS)*, IEEE: Washington, DC, USA, Sept. 6-9, 2017, 1.

(183) Evertsson, M.; Kjellman, P.; Cinthio, M.; Andersson, R.; Tran, T. A.; in't Zandt, R.; Grafström, G.; Toftevall, H.; Fredriksson, S.; Ingvar, C.; Strand, S.-E.; Jansson, T. Combined Magnetomotive Ultrasound, PET/CT, and MR Imaging of 68Ga-Labelled Superparamagnetic Iron Oxide Nanoparticles in Rat Sentinel Lymph Nodes *In Vivo*. *Sci. Rep.* **2017**, *7*, 4824.

(184) Mehrmohammadi, M.; Yoon, K. Y.; Qu, M.; Johnston, K. P.; Emelianov, S. Y. Enhanced Pulsed Magneto-Motive Ultrasound Imaging Using Superparamagnetic Nanoclusters. *Nanotechnology* **2011**, *22*, 45502.

(185) Holst, M.; Cinthio, M.; Fredriksson, S.; Olsson, F.; Persson, H. W.; Jansson, T. Phase-Locked Magnetomotive Ultrasound Imaging of Superparamagnetic Iron-Oxide Nanoparticles. In *2010 International Ultrasonics Symposium (IUS)*, IEEE: San Diego, USA, Oct. 11-14, 2010, 1007–1010.

(186) Hossain, M. M.; Levy, B. E.; Thapa, D.; Oldenburg, A. L.; Gallippi, C. M. Blind Source

Separation-Based Motion Detector for Imaging Super-Paramagnetic Iron Oxide (SPIO) Particles in Magnetomotive Ultrasound Imaging. *IEEE Trans. Med. Imaging* **2018**, *37*, 2356–2366.

(187) Fink, M.; Lyer, S.; Alexiou, C.; Rupitsch, S. J.; Ermert, H. Quantitative Imaging of the Iron-Oxide Nanoparticle- Concentration for Magnetic Drug Targeting Employing Inverse Magnetomotive Ultrasound. *Curr. Dir. Biomed. Eng.* **2019**, *5*, 417–419.

(188) Jansson, T.; Evertsson, M.; Atile, E.; Andersson, R.; Fredriksson, S.; Persson, H. W.; Svensson, I.; Cinthio, M. Induced Tissue Displacement in Magnetomotive Ultrasound Imaging - Simulations and Experiments. *IEEE Int. Ultrason. Symp. IUS* **2014**, 639–642.

(189) Ersepke, T.; Kranemann, T. C.; Schmitz, G. On the Performance of Time Domain Displacement Estimators for Magnetomotive Ultrasound Imaging. *IEEE Trans. Ultrason. Ferroelectr. Freq. Control* **2019**, *66*, 911–921.

(190) Pope, A. G.; Wu, G.; McWhorter, F. Y.; Merricks, E. P.; Nichols, T. C.; Czernuszewicz, T. J.; Gallippi, C. M.; Oldenburg, A. L. Contrast-Enhanced Imaging of SPIO-Labeled Platelets Using Magnetomotive Ultrasound. *Phys. Med. Biol.* **2013**, *58*, 7277–7290.

(191) Evertsson, M.; Ramalli, A.; Pavan, T. Z.; Cabrelli, L. C.; Andersson, R.; Cinthio, M.; Tortoli, P.; Jansson, T. Towards Real-Time Magnetomotive Ultrasound Imaging. In *IEEE International Ultrasonics Symposium, (IUS*), IEEE: Washington, DC, USA, Sept. 6-9, 2017, 1-4.

(192) Md Murad Hossain1, Diwash Thapa2, Justin Sierchio2, Amy Oldenburg2, and C.; Gallippil1. Blind Source Separation – Based Motion Detector for Sub- Micrometer, Periodic Displacement in Ultrasonic Imaging. *IEEE Int Ultrason Symp.* **2016**, *176*, 139–

148.

(193) Kranemann, T. C.; Ersepke, T.; Schmitz, G. Real-Time Magnetomotive Ultrasound Imaging Using a Recursive Estimator. *IEEE Int. Ultrason. Symp. IUS* **2018**, pp 1-4.

(194) Fink, M.; Ermert, H.; Lyer, S.; Alexiou, C. Influence of Naturally Occurring Tissue Movements on Magnetomotive Ultrasound Detection of Iron Oxide Nanoparticles for Magnetic Drug Targeting. *IEEE Int. Ultrason. Symp. IUS* **2017**, pp 1-6.

(195) Kruk, D.; Umut, E.; Masiewicz, E.; Sampl, C.; Fischer, R.; Spirk, S.; Goesweiner, C.; Scharfetter, H. 209Bi Quadrupole Relaxation Enhancement in Solids as a Step towards New Contrast Mechanisms in Magnetic Resonance Imaging. *Phys. Chem. Chem. Phys.* **2018**, *20*, 12710–12718.

(196) Gösweiner, C.; Lantto, P.; Fischer, R.; Sampl, C.; Umut, E.; Westlund, P. O.; Kruk, D.; Bödenler, M.; Spirk, S.; Petrovič, A.; Scharfetter, H. Tuning Nuclear Quadrupole Resonance: A Novel Approach for the Design of Frequency-Selective MRI Contrast Agents. *Phys. Rev. X* **2018**, *8*, 1–20.

(197) Kruk, D.; Masiewicz, E.; Umut, E.; Petrovic, A.; Kargl, R.; Scharfetter, H. Estimation of the Magnitude of Quadrupole Relaxation Enhancement in the Context of Magnetic Resonance Imaging Contrast. *J. Chem. Phys.* **2019**, *150*, 184306.

(198) Tay, Z. W.; Hensley, D. W.; Vreeland, E. C.; Zheng, B.; Conolly, S. M. The Relaxation Wall: Experimental Limits to Improving MPI Spatial Resolution by Increasing Nanoparticle Core Size. *Biomed. Phys. Eng. express* **2017**, *3*, 35003.

(199) Tay, Z. W.; Hensley, D. W.; Chandrasekharan, P.; Zheng, B.; Conolly, S. M. Optimization of Drive Parameters for Resolution, Sensitivity and Safety in Magnetic Particle Imaging.

IEEE Trans. Med. Imaging **2019**, *39*, 1724-1734.

(200) Li, D. S.; Schneewind, S.; Bruce, M.; Khaing, Z.; O'Donnell, M.; Pozzo, L. Spontaneous Nucleation of Stable Perfluorocarbon Emulsions for Ultrasound Contrast Agents. *Nano Lett.* **2018**, *19*, 173–181.

(201) Bourdeau, R.; Lee-Gosselin, A.; Lakshmanan, A.; Kumar, S.; Farhadi, A.; Shapiro, M. Acoustic Reporter Genes for Non-Invasive Imaging of Microbes in Mammalian Hosts. *Nat. Publ. Gr.* **2018**, *553*, 86–90.

(202) Sjostrand, S., Evertsson, M., Thring, C., Bacou, M., Farrington, S., Moug, S. Moran, C., Jansson, T., Mulvana, H. Contrast-Enhanced Magnetomotive Ultrasound Imaging (CE-MMUS) for Colorectal Cancer Staging: Assessment of Sensitivity and Resolution to Detect Alterations in Tissue Stiffness. *IEEE Int Ultrason Symp.* **2019**, 1077–1080.

(203) Hong, G.; Lee, J. C.; Robinson, J. T.; Raaz, U.; Xie, L.; Huang, N. F.; Cooke, J. P.; Dai, H. Multifunctional *In Vivo* Vascular Imaging Using Near-Infrared II Fluorescence. *Nat. Med.* **2012**, *18*, 1841–1846.

(204) Lim, Y. T.; Kim, S.; Nakayama, A.; Stott, N. E.; Bawendi, M. G.; Frangioni, J. V. Selection of Quantum Dot Wavelengths for Biomedical Assays and Imaging. *Mol. Imaging* **2003**, *2*, 50–64.

(205) He, Y.; Zhong, Y.; Su, Y.; Lu, Y.; Jiang, Z.; Peng, F.; Xu, T.; Su, S.; Huang, Q.; Fan, C.; Lee, S.-T. Water-Dispersed Near-Infrared-Emitting Quantum Dots of Ultrasmall Sizes for *In Vitro* and *In Vivo* Imaging. *Angew. Chem. Int. Ed.* **2011**, *50*, 5695–5698.

(206) Hines, M. A.; Scholes, G. D. Colloidal PbS Nanocrystals with Size-Tunable Near-Infrared Emission: Observation of Post-Synthesis Self-Narrowing of the Particle Size Distribution.

Adv. Mater. **2003**, *15*, 1844–1849.

(207) Cao; Banin, U. Growth and Properties of Semiconductor Core/Shell Nanocrystals with InAs Cores. *J. Am. Chem. Soc.* **2000**, *122*, 9692–9702.

(208) Gui, R.; Sun, J.; Liu, D.; Wang, Y.; Jin, H. A Facile Cation Exchange-Based Aqueous Synthesis of Highly Stable and Biocompatible Ag2S Quantum Dots Emitting in the Second near-Infrared Biological Window. *Dalt. Trans.* **2014**, *43*, 16690–16697.

(209) Gu, Y.-P.; Cui, R.; Zhang, Z.-L.; Xie, Z.-X.; Pang, D.-W. Ultrasmall Near-Infrared Ag2Se Quantum Dots with Tunable Fluorescence for *In Vivo* Imaging. *J. Am. Chem. Soc.* **2012**, *134*, 79–82.

(210) Weber, J.; Beard, P. C.; Bohndiek, S. E. Contrast Agents for Molecular Photoacoustic Imaging. *Nat. Methods* **2016**, *13*, 639–650.

(211) Abram, U. Innovative PET and SPECT Tracers. In *Quantification of Biophysical Parameters in Medical Imaging*; Sack, I., Schaeffter, T., Eds.; Springer International Publishing: Cham, 2018; pp 255–279.

(212) Pretze, M.; van der Meulen, N. P.; Wängler, C.; Schibli, R.; Wängler, B. Targeted 64Cu-Labeled Gold Nanoparticles for Dual Imaging with Positron Emission Tomography and Optical Imaging. *J. Label. Compd. Radiopharm.* **2019**, *62*, 471–482.

(213) Deberle, L. M.; Benešová, M.; Umbricht, C. A.; Borgna, F.; Büchler, M.; Zhernosekov, K.; Schibli, R.; Müller, C. Development of a New Class of PSMA Radioligands Comprising Ibuprofen as an Albumin-Binding Entity. *Theranostics* **2020**, *10*, 1678–1693.

(214) De La Vega, J. C.; Häfeli, U. O. Utilization of Nanoparticles as X-Ray Contrast Agents for Diagnostic Imaging Applications. *Contrast Media Mol. Imaging* **2015**, *10*, 81–95.

(215) Ahmad, M.; Pratx, G.; Bazalova, M.; Xing, L. X-Ray Luminescence and X-Ray Fluorescence Computed Tomography: New Molecular Imaging Modalities. *IEEE Access* **2014**, *2*, 1051–1061.

(216) Ashton, J. R.; West, J. L.; Badea, C. T. *In Vivo* Small Animal Micro-CT Using Nanoparticle Contrast Agents. *Front. Pharmacol.* **2015**, *6*, 256.

(217) Li, C.; Zhang, Y.; Wang, M.; Zhang, Y.; Chen, G.; Li, L.; Wu, D.; Wang, Q. *In Vivo* Real-Time Visualization of Tissue Blood Flow and Angiogenesis Using Ag2S Quantum Dots in the NIR-II Window. *Biomaterials* **2014**, *35*, 393–400.

(218) Wagener, P.; Jakobi, J.; Rehbock, C.; Chakravadhanula, V. S. K.; Thede, C.; Wiedwald, U.; Bartsch, M.; Kienle, L.; Barcikowski, S. Solvent-Surface Interactions Control the Phase Structure in Laser-Generated Iron-Gold Core-Shell Nanoparticles. *Sci. Rep.* **2016**, *6*, 23352.

(219) Jurado-Sánchez, B.; Escarpa, A.; Wang, J. Lighting up Micromotors with Quantum Dots for Smart Chemical Sensing. *Chem. Commun.* **2015**, *51*, 14088–14091.

(220) Toumia, Y.; Cerroni, B.; Trochet, P.; Lacerenza, S.; Oddo, L.; Domenici, F.; Paradossi, G. Performances of a Pristine Graphene-Microbubble Hybrid Construct as Dual Imaging Contrast Agent and Assessment of Its Biodistribution by Photoacoustic Imaging. *Part. Part. Syst. Charact.* **2018**, *35*, 1800066.

(221) Wang, L. V. Ultrasound-Mediated Biophotonic Imaging: A Review of Acousto-Optical Tomography and Photo-Acoustic Tomography. *Dis. Markers* **2004**, *19*, 478079.

(222) Resink, S. G.; Steenbergen, W.; Boccara, A. C. State-Of-The-Art of Acoust-Optic Sensing and Imaging of Turbid Media. *J. Biomed. Opt.* **2012**, *17*, 1–11.

(223) Debye, P.; Sears, F. W. On the Scattering of Light by Supersonic Waves. *Proc. Natl. Acad. Sci.* **1932**, *18*, 409–414.

(224) Radtke, U.; Zielke, R.; Rademacher, H.-G.; Crostack, H.-A.; Hergt, R. Application of Magneto-Optical Method for Real-Time Visualization of Eddy Currents with High Spatial Resolution for Nondestructive Testing. *Opt. Lasers Eng.* **2001**, *36*, 251–268.

(225) Zhou, Z.-F.; Cheng, Y.-H. Magneto-Optic Microscope for Visually Detecting Subsurface Defects. *Appl. Opt.* **2008**, *47*, 3463–3466.

(226) Cheng, Y.; Deng, Y.; Bai, L.; Chen, K. Enhanced Laser-Based Magneto-Optic Imaging System for Nondestructive Evaluation Applications. *IEEE Trans. Instrum. Meas.* **2013**, *62*, 1192–1198.

(227) Mariappan, L.; Shao, Q.; Jiang, C.; Yu, K.; Ashkenazi, S.; Bischof, J. C.; He, B. Magneto Acoustic Tomography with Short Pulsed Magnetic Field for *In Vivo* Imaging of Magnetic Iron Oxide Nanoparticles. *Nanomedicine Nanotechnology, Biol. Med.* **2016**, *12*, 689–699.

(228) Mariappan, L.; He, B. Magnetoacoustic Tomography with Magnetic Induction: Bioimepedance Reconstruction through Vector Source Imaging. *IEEE Trans. Med. Imaging* **2013**, *32*, 619–627.

(229) Podaru, G. V.; Chikan, V.; Prakash, P. Magnetic Field Induced Ultrasound from Colloidal Superparamagnetic Nanoparticles. *J. Phys. Chem. C* **2016**, *120*, 2386–2391.

(230) Dong, M.; Wang, X.; Chen, X.-Z.; Mushtaq, F.; Deng, S.; Zhu, C.; Torlakcik, H.; Terzopoulou, A.; Qin, X.-H.; Xiao, X.; Puigmartí-Luis, J.; Choi, H.; Pêgo, A. P.; Shen, Q.-D.; Nelson, B. J.; Pané, S. 3D-Printed Soft Magnetoelectric Microswimmers for Delivery and Differentiation of Neuron-Like Cells. *Adv. Funct. Mater.* **2020**, *30*, 1910323.

(231) Vellekoop, I. M. Feedback-Based Wavefront Shaping. *Opt. Express* **2015**, *23*, 12189-12206.

(232) Park, J. H.; Yu, Z.; Lee, K. R.; Lai, P.; Park, Y. K. Perspective: Wavefront Shaping Techniques for Controlling Multiple Light Scattering in Biological Tissues: Toward *In Vivo* Applications. *APL Photonics* **2018**, *3*, 100901.

(233) Ahn, C.; Hwang, B.; Nam, K.; Jin, H.; Woo, T.; Park, J. H. Overcoming the Penetration Depth Limit in Optical Microscopy: Adaptive Optics and Wavefront Shaping. *J. Innov. Opt. Health Sci.* **2019**, *12*, 1–18.

(234) Horstmeyer, R.; Ruan, H.; Yang, C. Guidestar-Assisted Wavefront-Shaping Methods for Focusing Light into Biological Tissue. *Nat. Photonics* **2015**, *9*, 563–571.

(235) Mosk, A. P.; Lagendijk, A.; Lerosey, G.; Fink, M. Controlling Waves in Space and Time for Imaging and Focusing in Complex Media. *Nat. Photonics* **2012**, *6*, 283–292.

(236) Vellekoop, I. M.; Cui, M.; Yang, C. Digital Optical Phase Conjugation of Fluorescence in Turbid Tissue. *Appl. Phys. Lett.* **2012**, *101*, 1–5.

(237) Koukourakis, N.; Fregin, B.; König, J.; Büttner, L.; Czarske, J. W. Wavefront Shaping for Imaging-Based Flow Velocity Measurements through Distortions Using a Fresnel Guide Star. *Opt. Express* **2016**, *24*, 22074–22087.

(238) Papadopoulos, I. N.; Jouhanneau, J. S.; Poulet, J. F. A.; Judkewitz, B. Scattering Compensation by Focus Scanning Holographic Aberration Probing (F-SHARP). *Nat. Photonics* **2017**, *11*, 116–123.

(239) Wang, Y. M.; Judkewitz, B.; Dimarzio, C. A.; Yang, C. Deep-Tissue Focal Fluorescence Imaging with Digitally Time-Reversed Ultrasound-Encoded Light. *Nat. Commun.* **2012**, *3*,

928.

(240) Judkewitz, B.; Wang, Y. M.; Horstmeyer, R.; Mathy, A.; Yang, C. Speckle-Scale Focusing in the Diffusive Regime with Time Reversal of Variance-Encoded Light (TROVE). *Nat. Photonics* **2013**, *7*, 300–305.

(241) Kong, L.; Cui, M. *In Vivo* Neuroimaging through the Highly Scattering Tissue *via* Iterative Multi-Photon Adaptive Compensation Technique. *Opt. Express* **2015**, *23*, 6145.

(242) Osnabrugge, G.; Amitonova, L. V.; Vellekoop, I. M. Blind Focusing through Strongly Scattering Media Using Wavefront Shaping with Nonlinear Feedback. *Opt. Express* **2019**, *27*, 11673.

(243) Yoon, J.; Lee, K.; Park, J.; Park, Y. Measuring Optical Transmission Matrices by Wavefront Shaping. *Opt. Express* **2015**, *23*, 10158.

(244) Conkey, D. B.; Caravaca-Aguirre, A. M.; Piestun, R. High-Speed Scattering Medium Characterization with Application to Focusing Light through Turbid Media. *Opt. Express* **2012**, *20*, 1733.

(245) Shen, Y.; Liu, Y.; Ma, C.; Wang, L. V. Focusing Light through Biological Tissue and Tissue-Mimicking Phantoms up to 9.6 Cm in Thickness with Digital Optical Phase Conjugation. *J. Biomed. Opt.* **2016**, *21*, 085001.

(246) Jang, M.; Ruan, H.; Vellekoop, I. M.; Judkewitz, B.; Chung, E.; Yang, C. Relation between Speckle Decorrelation and Optical Phase Conjugation (OPC)-Based Turbidity Suppression through Dynamic Scattering Media: A Study on *In Vivo* Mouse Skin. *Biomed. Opt. Express* **2015**, *6*, 72-85.

(247) Katz, O.; Heidmann, P.; Fink, M.; Gigan, S. Non-Invasive Single-Shot Imaging through

Scattering Layers and around Corners *via* Speckle Correlations. *Nat. Photonics* **2014**, *8*, 784–790.

(248) Cua, M.; Zhou, E. (Haojiang); Yang, C. Imaging Moving Targets through Scattering Media. *Opt. Express* **2017**, *25*, 3935-3945.

(249) Bertolotti, J.; van Putten, E. G.; Blum, C.; Lagendijk, A.; Vos, W. L.; Mosk, A. P. Non-Invasive Imaging through Opaque Scattering Layers. *Nature* **2012**, *491*, 232–234.

(250) Yang, X.; Pu, Y.; Psaltis, D. Imaging Blood Cells through Scattering Biological Tissue Using Speckle Scanning Microscopy. *Opt. Express* **2014**, *22*, 3405-3413.

(251) Kuschmierz, R.; Scharf, E.; Koukourakis, N.; Czarske, J. W. Self-Calibration of Lensless Holographic Endoscope Using Programmable Guide Stars. *Opt. Lett.* **2018**, *43*, 2997–3000.

(252) Stasio, N.; Moser, C.; Psaltis, D. Calibration-Free Imaging through a Multicore Fiber Using Speckle Scanning Microscopy. *Opt. Lett.* **2016**, *41*, 3078-3081.

Table of Content Image